Monthly Notices
of the
ROYAL ASTRONOMICAL SOCIETY

MNRAS **528,** 5763–5782 (2024)
Advance Access publication 2024 January 30

https://doi.org/10.1093/mnras/stae268

Mapping dust in the giant molecular cloud Orion A

Amery Gration[1,2]★ and John Magorrian[1]
[1]*Rudolf Peierls Centre for Theoretical Physics, Beecroft Building, Parks Road, Oxford, OX1 3PU, UK*
[2]*Department of Physics, University of Surrey, Guildford, GU2 7XH, UK*

Accepted 2024 January 18. Received 2024 January 17; in original form 2023 May 22

ABSTRACT

The Sun is located close to the Galactic mid-plane, meaning that we observe the Galaxy through significant quantities of dust. Moreover, the vast majority of the Galaxy's stars also lie in the disc, meaning that dust has an enormous impact on the massive astrometric, photometric and spectroscopic surveys of the Galaxy that are currently underway. To exploit the data from these surveys we require good three-dimensional maps of the Galaxy's dust. We present a new method for making such maps in which we form the best linear unbiased predictor of the extinction at an arbitrary point based on the extinctions for a set of observed stars. This method allows us to avoid the artificial inhomogeneities (so-called 'fingers of God') and resolution limits that are characteristic of many published dust maps. Moreover, it requires minimal assumptions about the statistical properties of the interstellar medium. In fact, we require only a model of the first and second moments of the dust density field. The method is suitable for use with directly measured extinctions, such as those provided by the Rayleigh–Jeans colour excess method, and inferred extinctions, such as those provided by hierarchical Bayesian models like StarHorse. We test our method by mapping dust in the region of the giant molecular cloud Orion A. Our results indicate a foreground dust cloud at a distance of 350 pc, which has been identified in work by another author.

Key words: ISM: clouds – dust, extinction – ISM: structure – local interstellar matter – solar neighbourhood.

1 INTRODUCTION

The giant molecular clouds Orion A and B are sites of continuing star formation. Indeed, they are the regions closest to Earth in which high-mass ($M > 8\,\mathrm{M}_\odot$) star formation is occurring. Both Orion A and B are filamentary structures. Orion A, which is comet-like, consists of a dense head (containing the Orion Nebula, at galactic coordinates $l = 206$ deg, $b = -16.4$ deg, and its largest cluster of young stars, the Orion Nebula Cluster) and a diffuse tail extending south-west on the sky for several degrees. Orion B is more uniform. It contains the Flame Nebula at its eastern extremity (at galactic coordinates $l = 209$ deg, $b = -19.4$ deg) and extends north-west on the sky, again for several degrees.

Photometric surveys of young stars and young stellar objects, which trace the gas of the molecular cloud in which they have been concieved and born, have charted the gross on-sky distribution of Orion A. These surveys include those by: Meingast et al. (2016), Meingast, Alves & Lombardi (2018), and Großschedl et al. (2019), as part of the VISION surveys, which used near-infrared observations made by the VISTA telescope augmented by visible and near-infrared observations by Pan-STARRS and mid-infrared observations by Spitzer; Megeath et al. (2012, 2015), which used mid-infrared observations made by Spitzer and near-infrared observations made by 2MASS; Carpenter (2000), which used near-infrared observations made by 2MASS; and Wright et al. (2010), which used mid-infrared observations by WISE. Astrometric surveys of the same young stars and young stellar objects have allowed us to chart the gross three-dimensional distribution of Orion A. These surveys include those by Kounkel et al. (2018) and Großschedl et al. (2018), using *Gaia* Data Release 2 (DR2). They have established that the head of Orion A is a roughly spherical object, with a diameter of 15–20 pc, lying at a distance of $s = 400$ pc at $l = 209$ deg, $b = -19.5$ deg, and that its tail extends away from the Sun for a distance of 75 pc at an angle of 70 deg to the plane of the sky.

To chart the fine three-dimensional distribution of Orion A we can use dust, which is coupled to the gas component of the interstellar medium (ISM) and hence traces the densest gas of the molecular cloud in which it sits. The dust is accessible to us by its extincting effect on light passing through it. But the task of charting the dust of Orion A is very different from the task of charting its stellar population. It is a matter of inference rather than direct observation. Given extinctions for stars in the region of Orion A we can *infer* the dust density at an arbitrary point in the cloud, a process known as 'three-dimensional dust mapping'. A number of teams have already made three-dimensional dust maps of Orion A. These include: Schlafly et al. (2015), using only photometry from Pan-STARRS1; Rezaei Kh et al. (2018), using astrometry from *Gaia* Data Release 1 together with photometry from 2MASS and WISE, Rezaei Kh et al. (2020), using astrometry from *Gaia* DR2 together with photometry from 2MASS and WISE; and Dharmawardena et al. (2022), using astrometry from *Gaia* DR2 together with photometry from 2MASS, WISE, and *Gaia* DR2. All three identify a filament of gas consistent with the tail of young stellar objects and young stars. Rezaei Kh et al. (2020) report a cloud lying in the foreground of Orion A, at a distance of $s = 350$ pc, which they tentatively associate with a stellar

---

★ E-mail: a.gration@surrey.ac.uk

cluster identified by Bouy et al. (2014). However, this cloud is not reported by either of the other two groups.

Although the distributions of the gas and dust are of interest in their own right, the dust is also something of a nuisance since it obscures and reddens observations of stars within and beyond it. Because the Sun is located close to the Galactic mid-plane we observe our Galaxy through significant quantities of dust. Moreover, the vast majority of the Galaxy's stars also lie in the disc, so extinction has an enormous impact on stellar surveys and, in turn, on attempts to fit chemical and dynamical models of the Galaxy to stellar observations. To fully exploit the data from stellar surveys we require good three-dimensional dust maps of the whole Galaxy. A number of teams have made such three-dimensional dust maps. These include: Arenou, Grenon & Gomez (1992); Drimmel, Cabrera-Lavers & López-Corredoira (2003); Marshall et al. (2006); Sale et al. (2014; based on the method of Sale 2012); Chen et al. (2014; based on the method of Berry et al. 2012); Lallement (2015), Lallement et al. (2014, 2018, 2019), and Vergely et al. (2010; based on the method of Vergely et al. 2001); Green et al. (2015, 2018, 2019; based on the method of Green et al. 2014); and Leike & Enßlin (2019), and Leike, Glatzle & Enßlin (2020; based on the method of Enßlin & Weig 2010) and Enßlin & Frommert (2011).

To date, however, dust maps have suffered from either artificial inhomogenities known as 'fingers of God' (Marshall et al. 2006; Green et al. 2018; Lallement et al. 2019), or have been resolution-limited (Sale et al. 2014; Leike, Glatzle & Enßlin 2020; Rezaei Kh et al. 2020). We propose a new method for creating three-dimensional dust maps and use it to map Orion A. Orion A is a good testing ground for dust-mapping methods that might be used to map the whole Galaxy.

When making a three-dimensional dust map we wish to infer the density, $\rho(\boldsymbol{r})$ or, equivalently, the extinction, $A(\boldsymbol{r})$, at an arbitrary point, $\boldsymbol{r}$, given knowledge of the positions, $\boldsymbol{r}_1, \dots, \boldsymbol{r}_n$, and extinctions, $A_1, \dots, A_n$ for some set of stars. In this paper we treat the ISM as the realization of a random field, and compute the best linear unbiased predictor (BLUP) of the extinction at a point given extinctions for a set of stars in the region of that point. This is equivalent to forming the generalized least squares estimator of the mean of the extinction and then performing a non-parameteric fit to the residuals. We then differentiate this predictor to give a predictor of the density at the same point. Our method requires minimal assumptions about the statistical properties of the ISM. Indeed it requires us to know only the covariance of the densities of the ISM and to have a model of its mean. It does not require us to assume a distribution for the dust density, and in particular it does not require us to assume a log-normal distribution, as is common in three-dimensional dust mapping. We follow Sale & Magorrian (2014) in using a physically motivated model of the covariance function that captures the turbulent structure of the ISM. The parameters of this covariance model form the hyperparameters of our predictor of extinction, which we optimize using the method of leave-one out cross validation. We make two maps of dust in the region of Orion A out to 500 pc: one using extinctions computed using the Rayleigh–Jeans colour excess method, and one using extinctions from the StarHorse catalague. The resulting maps display no fingers of God, and may be constructed at arbitrary resolution although the effective resolution is always limited by the density of observed stars.

Our method relies on knowledge of only the broadest statistical properties of the density field (i.e. its first and second moments) and we begin, in Section 2, by summarizing these. We then introduce the BLUP, in Section 3, testing it against simulated data in Section 4 before using it to map Orion A, in Section 5. Our maps broadly agree with those made by Rezaei Kh et al. (2020) and, like them, show a foreground dust cloud at a distance of 350 pc. In Section 6 we discuss the consequences of our assumptions about the statistical properties of the density field and show that our method is insensitive to them so long as they correctly account for the fractal nature of the ISM.

2 STATISTICS OF THE ISM

The density of the ISM at a point, $\boldsymbol{r}$, may be represented by the random variable, $\rho(\boldsymbol{r})$. The set of all such random variables forms a random field, $\rho := (\rho(\boldsymbol{r}))_{\boldsymbol{r}\in\mathbf{R}^3}$, which represents the density of the ISM as a whole. Similarly, the extinction of light emitted by a source at a point, $\boldsymbol{r}$, may be represented by the random variable

$$A(\boldsymbol{r}) = \int_0^s \rho(s'\hat{\boldsymbol{r}})\,\mathrm{d}s' \tag{1}$$

where $s := |\boldsymbol{r}|$ is the line-of-sight distance of the source and $\hat{\boldsymbol{r}}$ is the unit vector parallel to $\boldsymbol{r}$. This gives another random field, $A := (A(\boldsymbol{r}))_{\boldsymbol{r}\in R^3}$, which represents the extinction that would be undergone by light emitted at any point in space. The properties of these fields are usefully summarized by their means and variances. Since the expectation and covariance functions are both linear we immediately find that the expectation of $A(\mathbf{r})$ is

$$\langle A(\boldsymbol{r})\rangle = \left\langle \int_0^s \rho(s'\hat{\boldsymbol{r}})\,\mathrm{d}s' \right\rangle \tag{2}$$

$$= \int_0^s \left\langle \rho(s'\hat{\boldsymbol{r}})\right\rangle \mathrm{d}s' \tag{3}$$

and that the covariance of $A(\mathbf{r})$ is[1]

$$\operatorname{cov}(A(\boldsymbol{r}_i), A(\boldsymbol{r}_j)) = \operatorname{cov}\left(\int_0^{s_i} \rho(s_i'\hat{\boldsymbol{r}}_i)\,\mathrm{d}s_i', \int_0^{s_j} \rho(s_j'\hat{\boldsymbol{r}}_j)\,\mathrm{d}s_j',\right) \tag{4}$$

$$= \int_0^{s_j}\int_0^{s_i} \operatorname{cov}(\rho(s_i'\hat{\boldsymbol{r}}_i), \rho(s_j'\hat{\boldsymbol{r}}_j))\,\mathrm{d}s_i'\,\mathrm{d}s_j', \tag{5}$$

where $s_i := |\boldsymbol{r}_i|$ and $s_j := |\boldsymbol{r}_j|$ are the line-of-sight distances of the two sources and $\hat{\boldsymbol{r}}_i$ and $\hat{\boldsymbol{r}}_j$ are the unit vectors parallel to $\boldsymbol{r}_i$ and $\boldsymbol{r}_j$. Although the ISM is a complicated multiphase medium, the fluctuation in its density,

$$\Delta\rho := \rho - \langle\rho\rangle\,, \tag{6}$$

can be approximated as being stationary and isotropic (Draine 2011). In these circumstances, its first and second moments are invariant under translations and rotations. Consequently, the covariance of the density fluctuations at two points, $\Delta\rho(\boldsymbol{r}_i)$ and $\Delta\rho(\boldsymbol{r}_j)$, is a function of their separation, $|\boldsymbol{r}_j - \boldsymbol{r}_i|$, and is given by the *autocovariance function* of the density fluctuations, $k_{\Delta\rho}$, such that

$$k_{\Delta\rho}(|\boldsymbol{r}_j - \boldsymbol{r}_i|) = \operatorname{cov}(\Delta\rho(\boldsymbol{r}_i), \Delta\rho(\boldsymbol{r}_j)). \tag{7}$$

By Bochner's Theorem (Adler 1981) the Fourier transform of $k_{\Delta\rho}$ exists, and is related to the *power spectrum* of $\Delta\rho$, denoted $P_{\Delta\rho}$, via the equation

$$k_{\Delta\rho}(|\boldsymbol{r}_j - \boldsymbol{r}_i|) = \int_{R^3} \mathrm{e}^{\mathrm{i}\boldsymbol{k}\cdot(\boldsymbol{r}_j - \boldsymbol{r}_i)} P_{\Delta\rho}(|\boldsymbol{k}|)\,\mathrm{d}|\boldsymbol{k}|, \tag{8}$$

where $\boldsymbol{k}$ is the three-dimensional wavenumber.

It is common to assume that fluctuations in the density are described by Kolmogorov's theory of turbulence (Draine 2011), i.e. that its power spectrum is described by a power law, with index

---

[1] What Sale & Magorrian (2014, equation A2) call the correlation, $\langle A(\boldsymbol{s}_1)A(\boldsymbol{s}_2)\rangle$, should be the covariance, $\operatorname{cov}(A(\boldsymbol{s}_1), A(\boldsymbol{s}_2))$.

$-11/3$, over a wide range of wavenumbers.[2] This power law must fail at very small and very large wavenumbers. In the Kolmogorov theory of turbulence this happens at the boundaries of the inertial regime, i.e. at scales larger than the energy-injection scale, L_0, or smaller than the dissipation scale. The energy-injection scale is that of stellar feedback, while the energy-dissipation scale is that of viscous forces. Although astronomical observations clearly probe the energy-injection scale, they do not probe the energy-dissipation scale, meaning that we need only worry about the failure of the power-law power spectrum for small wavenumbers. Motivated by this fact, Sale & Magorrian (2014) proposed a split-power law for the power spectrum of $\Delta\rho$, with the location of the break being determined by the energy-injection scale, L_0. It is given by

$$P_{\Delta\rho}(|\boldsymbol{k}|) = \sigma^2_{\Delta\rho} R \frac{(|\boldsymbol{k}|L_0)^{2\Omega}}{(1+(|\boldsymbol{k}|L_0)^2)^{\gamma/2+\Omega}} \tag{9}$$

for positive numbers Ω, γ, and R, a normalizing constant defined implicitly by the equation

$$\frac{1}{R} = 4\pi \int_0^\infty \frac{|\boldsymbol{k}|^2(|\boldsymbol{k}|L_0)^{2\Omega}}{(1+(|\boldsymbol{k}|L_0)^2)^{\gamma/2+\Omega}}\,\mathrm{d}|\boldsymbol{k}|. \tag{10}$$

Above the wavelength associated with the energy-injection scale, L_0, the spectrum is a power-law with index $-\gamma$, and below that wavelength it is a power law with index Ω. Sale & Magorrian call this power spectrum 'Kolmogorov-like', regardless of the value of γ.

The mean value of the density is in general unknown, but its covariance is equal to the covariance of the density fluctuations, since

$$\mathrm{cov}(\rho(\boldsymbol{r}_i), \rho(\boldsymbol{r}_j)) = \left\langle(\rho(\boldsymbol{r}_i) - \langle\rho(\boldsymbol{r}_i)\rangle)(\rho(\boldsymbol{r}_j) - \left\langle\rho(\boldsymbol{r}_j)\right\rangle)\right\rangle \tag{11}$$

$$= \mathrm{cov}(\Delta\rho(\boldsymbol{r}_i), \Delta\rho(\boldsymbol{r}_j)). \tag{12}$$

The density, ρ, is often taken to be lognormal, meaning that the extinction at a point, $A(\boldsymbol{r})$, is the integral of a lognormal field. This has a probability density function (PDF) that cannot be expressed in closed form, but which is itself approximately lognormal (Ostriker, Stone & Gammie 2001).

If we assume that the density (as well as its fluctuations)[3] is stationary and isotropic, with mean μ_ρ and constant variance σ^2_ρ then the covariance of the densities at two points, $\rho(\boldsymbol{r}_i)$ and $\rho(\boldsymbol{r}_j)$, is also a function of their separation, $|\boldsymbol{r}_j - \boldsymbol{r}_i|$, and is given by the autocovariance function of the density, k_ρ, such that

$$k_\rho(|\boldsymbol{r}_j - \boldsymbol{r}_i|) = \mathrm{cov}(\rho(\boldsymbol{r}_i), \rho(\boldsymbol{r}_j)). \tag{13}$$

The autocovariance of the density is then equal to the autocovariance of the density fluctuations, i.e. $k_\rho = k_{\Delta\rho}$, and we have that

$$\langle A(\boldsymbol{r})\rangle = \mu_\rho s, \tag{14}$$

$$\mathrm{cov}(A(\boldsymbol{r}_i), A(\boldsymbol{r}_j)) = \int_0^{s_i}\int_0^{s_j} k_{\Delta\rho}(|s_i'\hat{\boldsymbol{r}}_i - s_j'\hat{\boldsymbol{r}}_j|)\,\mathrm{d}s_j'\,\mathrm{d}s_i' \tag{15}$$

where $k_{\Delta\rho}$ is given by equations (8) and 9. For each choice of autocovariance function, we need only a model of the mean of the extinction, which has a single free parameter, μ_ρ. Despite this simplifying assumption, neither $\mathrm{cov}(A(\boldsymbol{r}_i), A(\boldsymbol{r}_j))$ nor $\mathrm{cov}(\rho(\boldsymbol{r}_i), A(\boldsymbol{r}_j))$ has closed form, and both must be computed numerically at some expense. For this reason we define the functions f and g such that

$$f(s_1, s_2, \theta_{12}) = \mathrm{cov}(\rho(\boldsymbol{r}_1), \rho(\boldsymbol{r}_2)) \tag{16}$$

$$g(s_1, s_2, \theta_{12}) = \mathrm{cov}(A(\boldsymbol{r}_1), A(\boldsymbol{r}_2)) \tag{17}$$

where s_1 and s_2 are the line-of-sight distances to points $\boldsymbol{r}_1$ and $\boldsymbol{r}_2$, and θ_{12} is the angle subtended by them at the origin, which we precompute on a regular lattice of arguments and evaluate using linear interpolation. (We discuss these functions further in Appendix D.)

3 LINEAR PREDICTION AND MAP MAKING

When making a three-dimensional dust map we wish to infer the density or, equivalently, the extinction at an arbitrary point given knowledge of the extinctions and positions for some set of stars. Of course, neither the distance nor the extinction are observed directly. Instead, they must themselves be inferred from other stellar properties. For a limited number of stars (those for which we have observations in the infrared) we may estimate the extinction using the near-infrared colour excess (NICE) method of Lada et al. (1994) or its successors [the NICER method due to Lombardi & Alves (2001), the NICEST method due to Lombardi (2009), and the Rayleigh–Jeans colour excess method due to Majewski, Zasowski & Nidever (2011)]. The Rayleigh–Jeans colour excess (RJCE) method, for example, exploits the fact that all stars are well approximated as black bodies in the low-frequency limit (where their spectral radiance is described by the Rayleigh–Jeans law), meaning that their low-frequency colours are approximately independent of spectral class. Majewski, Zasowski & Nidever (2011) showed that colours spanning the NIR and MIR are approximately constant for a range of spectral types, and that the colour $H - [4.5\ \mu]$ exhibits especially little variation. They found, using the extinction law of Cardelli, Clayton & Mathis (1989), that the K_s-band extinction in magnitudes is

$$A_{K_\mathrm{s}} = 0.918(H - [4.5\ \mu] - 0.08) \tag{18}$$

with a scatter of 0.1 mag for F, G, and K stars, and 0.4 mag for B–M excluding late type dwarfs. However, due to observational error, both distances and extinctions estimated in this way may be unphysically negative.

However, it is often necessary to infer the extinction and distance of a star using Bayesian methods of the kind pioneered by Burnett & Binney (2010), Bailer-Jones (2011), and Binney et al. (2014). These methods assume that a star's observed properties are parametrized by its intrinsic properties, and use Bayes's theorem to compute the posterior PDF of the intrinsic properties given the observed properties. We might wish to infer a single property or a tuple of properties, in which case we can find the marginal PDF of any element of that tuple. Several catalogues of stellar properties have been compiled in this way. They include the StarHorse catalogue (Santiago et al. 2016; Queiroz et al. 2018; Anders et al. 2019, 2021), and the catalogues of Bailer-Jones and his collaborators (Bailer-Jones 2015; Astraatmadja & Bailer-Jones 2016a, b; Bailer-Jones et al. 2018, 2021).

The StarHorse catalogue takes the intrinsic properties of a star to be mass, age, distance, and V-band extinction. It takes the observable properties of a star to be effective temperature, surface gravity, overall metallicity, magnitude, and parallax, as catalogued by *Gaia*,

---

[2] This is a remarkable fact since Kolmogorov's theory of turbulence describes the behaviour of small-amplitude incompressible hydrodynamic systems, and the ISM is a large-amplitude compressible magnetohydrodynamic system (Draine 2011).

[3] Of course the density of the ISM decreases exponentially as Galactic radius increases. Moreover, at large scales, the ISM forms complex sheet-like and filamentary structures. At these large scales the assumptions of stationary density and stationary density fluctuations are poor. However, at the small scales we consider in this paper both assumptions are reasonable.

Pan-STARRS1, 2MASS, and AllWISE. The likelihood of these observable properties is assumed to be Gaussian with mean given by a stellar model, and variance given by the observational errors. It assumes as a prior PDF for distance a physically motivated four-component model of the Galaxy (comprising the thin disc, thick disc, bulge/bar, and halo). As a result, inferred distances are always positive. In the first release of the StarHorse catalogue, using *Gaia* DR2 (Anders et al. 2019), the prior PDF for extinctions is assumed to be uniform in the case of stars with low-noise parallax observations (signal-to-noise of five or greater) and a top hat, such that $A_V/\mathrm{mag} \in [-0.3, 4]$, in the case of stars with high-noise parallax observations (signal-to-noise of less than five). In the second release, using *Gaia* Early Data Release 3 (EDR3; Anders et al. 2021), the prior PDF for extinctions is assumed to be given by the maps of Green et al. (2019) or Drimmel, Cabrera-Lavers & López-Corredoira (2003) according to coverage. The full posterior PDF is not publicly available, but rather the 0.05, 0.16, 0.6, 0.84, and 0.95 quantiles.

The catalogues of Bailer-Jones provide only distances. They take the intrinsic property of a star to be distance, and its observable property to be parallax. The most recent of these catalogues (Bailer-Jones et al. 2018, 2021) assumes that the likelihood of the parallax is Gaussian with mean given by the reciprocal distance and variance given by the observational errors, and that the prior PDF for distance is that for a generalized gamma distribution. As a result, inferred distances are again always positive. Again, the full posterior PDF is not publicly available, but rather the 0.05, 0.16, 0.6, 0.84, and 0.95 quantiles.

3.1 The BLUP

For a list of directly computed or inferred extinctions $\boldsymbol{A} = (A_1, \dots, A_n)$ at locations $\boldsymbol{r}_1, \dots, \boldsymbol{r}_n$ we wish to predict the extinction, $A(\boldsymbol{r})$, or density, $\rho(\boldsymbol{r})$, at some arbitrary position, $\boldsymbol{r}$, given the assumptions represented by equations (14) and 15. To predict the extinction we will use the BLUP of $A(\boldsymbol{r})$, which we will denote $\hat{A}(\boldsymbol{r})$. This is a linear combination of extinctions $A_1, \dots, A_n$ with coefficients chosen so as to minimize the mean square error,

$$\mathrm{MSE}(\hat{A}(\boldsymbol{r})) = \left\langle (A(\boldsymbol{r}) - \hat{A}(\boldsymbol{r}))^2 \right\rangle \tag{19}$$

(where angle brackets again indicate the expectation) subject to the constraint that $\hat{A}(\boldsymbol{r})$ be unbiased, i.e. subject to the constraint that $\langle \hat{A}(\boldsymbol{r}) \rangle = \langle A(\boldsymbol{r}) \rangle$. It is given by Goldberger (1962) as

$$\hat{A}(\boldsymbol{r}) = \boldsymbol{\gamma}(\boldsymbol{r})^{\mathrm{t}} \boldsymbol{A} + \sigma(\boldsymbol{r})^{\mathrm{t}} \boldsymbol{\Sigma}^{-1} (\boldsymbol{A} - \boldsymbol{\Gamma}^{\mathrm{t}} \boldsymbol{A}) \tag{20}$$

where the $n \times 1$ vector-valued function $\boldsymbol{\gamma}$ is given by

$$\boldsymbol{\gamma}(\boldsymbol{r}) = \boldsymbol{\Sigma}^{-1} \Phi^{\mathrm{t}} (\Phi \boldsymbol{\Sigma}^{-1} \Phi^{\mathrm{t}})^{-1} s, \tag{21}$$

the $n \times 1$ vector-valued function σ is given element-wise by $[\sigma(\boldsymbol{r})]_i = \mathrm{cov}(A(\boldsymbol{r}), A_i)$, the $n \times n$ matrix $\boldsymbol{\Sigma}$ has elements $[\boldsymbol{\Sigma}]_{ij} = \mathrm{cov}(A_j, A_i)$, the $n \times n$ matrix $\boldsymbol{\Gamma}$ has columns $[\boldsymbol{\Gamma}]_j = \boldsymbol{\gamma}(\boldsymbol{r}_j)$, meaning that it has elements $[\boldsymbol{\Gamma}]_{ij} = [\boldsymbol{\gamma}(\boldsymbol{r}_j)]_i$, and the $n \times 1$ vector $\boldsymbol{\Phi}$ has elements $[\boldsymbol{\Phi}]_i = s_i$.

The expression for $\hat{A}(\boldsymbol{r})$ is the sum of two terms. The first of these, $\boldsymbol{\gamma}(\boldsymbol{r})^{\mathrm{t}} \boldsymbol{A}$, is the generalized least squares (GLS) estimator of the mean of $A(\boldsymbol{r})$, which we may rewrite as $\hat{\mu}_\rho s$, where

$$\hat{\mu}_\rho := (\boldsymbol{\Phi}^{\mathrm{t}} \boldsymbol{\Sigma}^{-1} \boldsymbol{\Phi})^{-1} \boldsymbol{\Phi} \boldsymbol{\Sigma}^{-1} \boldsymbol{A} \tag{22}$$

is itself the GLS estimator of the mean of the density, μ_ρ, and is unbiased. Similarly, the expression $\boldsymbol{\Gamma}^{\mathrm{t}} \boldsymbol{A}$ gives the GLS estimators of the means of $A_1, \dots, A_n$. The second term in the expression for $\hat{A}(\boldsymbol{r})$ is then a weighted sum of the residuals of the observed values $\boldsymbol{A}$ and the GLS of their means.[4]

To predict the density we will use the derivative of the BLUP of $A(\boldsymbol{r})$,

$$\hat{\rho}(\boldsymbol{r}) := \frac{\partial \hat{A}(\boldsymbol{r})}{\partial s}, \tag{23}$$

which is also unbiased, since $\langle \rho(\boldsymbol{r}) - \hat{\rho}(\boldsymbol{r}) \rangle = \langle \partial (A(\boldsymbol{r}) - \hat{A}(\boldsymbol{r})) / \partial s \rangle = \partial \left\langle A(\boldsymbol{r}) - \hat{A}(\boldsymbol{r}) \right\rangle / \partial s = 0$. Because only $\boldsymbol{\gamma}$ and σ are functions of s it is easy to compute (see Appendix A for details).

Note that to find $\hat{A}(\boldsymbol{r})$ and $\hat{\rho}(\boldsymbol{r})$ we need only to know the covariance of $(A(\boldsymbol{r}), \boldsymbol{A})$ and to assume that the expectation of $A(\boldsymbol{r})$ is linear in s. We do not need to make any further assumptions about the distribution of the ISM. In particular, we do not need to assume that its distribution is lognormal.[5]

3.1.1 Computing the BLUP in practice

When using extinctions inferred with the RJCE method we can make the decomposition $A_i = A(\boldsymbol{r}_i) + E_i$ where $A(\boldsymbol{r}_i)$ is the intrinsic extinction at $\boldsymbol{r}_i$ and E_i is the uncertainty in its value. In this case the covariance matrix is

$$[\boldsymbol{\Sigma}]_{ij} = \mathrm{cov}(A(\boldsymbol{r}_i) + E_i, A(\boldsymbol{r}_j) + E_j) \tag{24}$$

$$= \mathrm{cov}(A(\boldsymbol{r}_i), A(\boldsymbol{r}_j)) + \mathrm{var}(E_i)\delta_{ij}, \tag{25}$$

assuming that $A(\boldsymbol{r}_i)$ and E_j are independent for $i \neq j$, and

$$[\sigma(\boldsymbol{r})]_i = \mathrm{cov}(A(\boldsymbol{r}), A(\boldsymbol{r}_i) + E_i) \tag{26}$$

$$= \mathrm{cov}(A(\boldsymbol{r}), A(\boldsymbol{r}_i)), \tag{27}$$

assuming that $A(\boldsymbol{r})$ and E_j are independent. When using extinctions inferred by Bayesian techniques that make stronger assumptions about he stars' neighbourhoods A_i is the posterior prediction of a source's extinction, and both $\mathrm{cov}(A_i, A_j)$ and $\mathrm{cov}(A(\boldsymbol{r}), A_i)$ are properties of the Bayesian model used to construct it. Since neither is available as part of a catalogue we will approximate them by equations (25) and (27), on the understanding that $\mathrm{var}(E_i)\delta_{ij}$ no longer represents an observational error but instead quantifies the discrepancy between our approximation of the covariance and its true value. We will take $\mathrm{var}(E_i)$ to be equal to the variance of $\mathrm{var}(A_i)$.

To compute $\hat{A}(\boldsymbol{r})$ we must know the position of each star. However, as we have already noted, the distance to a star is inherently uncertain. To circumvent this problem we may assume that the distance to a star is certain but that the uncertainty in the extinction is increased, using the fact that

$$\mathrm{d}A_i = \frac{\partial A_i}{\partial s_i} \Delta s_i. \tag{28}$$

In this case, the variance of A_i is increased by $\mathrm{d}A_i^2$. Under this assumption the *ij*-th element covariance matrix, $[\boldsymbol{\Sigma}]_{ij}$, becomes $[\boldsymbol{\Sigma}]_{ij} + \mathrm{d}A_i^2 \delta_{ij}$, i.e. we add the square of the uncertainties,

---

[4] A similar method of prediction, known as 'kriging' is much used in the mining industry for mapping geological features (see e.g. Cressie 1993).

[5] Our expression for $\hat{A}(\boldsymbol{r})$ is identical to that used in Gaussian-process emulation, where it would be derived under the assumption that $A(\boldsymbol{r})$ and $\boldsymbol{A}$ are drawn from an underlying Gaussian random field (e.g. Rasmussen 2006). However this assumption of Gaussianity is unnecessary. The expression holds because the random field A is second order, not because A is Gaussian (which it need not be).

$\mathrm{d}A_1, \ldots, \mathrm{d}A_n$, to the diagonal elements of $\mathbf{\Sigma}$. If $\mathrm{d}s_i \ll L_0$ then we may make the linear approximation,

$$\frac{\partial A_i}{\partial s_i} = \frac{A_i}{s_i}. \tag{29}$$

Of course, if the condition $\mathrm{d}s_i \ll L_0$ is not met then this additional term in the variance will be too great.

3.2 Validation

Although our statistical model of the ISM is physically motivated, we would still like reassurance that $\hat{A}(\boldsymbol{r})$ and $\hat{\rho}(\boldsymbol{r})$ are good predictors of $A(\boldsymbol{r})$ and $\rho(\boldsymbol{r})$. In the case of extinction we may test the performance of the BLUP using leave-one-out cross-validation (LOOCV). We partition $\boldsymbol{A}$ into a set containing a single element, A_i, and another containing $n-1$ elements, $\boldsymbol{A}_{-i} := (A_1, \ldots, A_{i-1}, A_{i+1}, \ldots, A_n)$. We then find $\hat{A}(\boldsymbol{r}_i)$, namely the BLUP of $A(\boldsymbol{r}_i)$ based on $\boldsymbol{A}_{-i}$, and compute the residual, $A_i - \hat{A}(\boldsymbol{r}_i)$. The behaviour of these n residuals should be consistent with the assumptions we have made about their distribution. Since we have only assumed that the mean is linear and that we know the autocovariance function, we need only check that the residuals obey Chebyshev's inequality,

$$\Pr(|A(\boldsymbol{r}) - \hat{A}(\boldsymbol{r})| \geq \lambda \,\mathrm{std}(A(\boldsymbol{r}) - \hat{A}(\boldsymbol{r})) \leq \frac{1}{\lambda^2} \tag{30}$$

where $\mathrm{std}(A(\boldsymbol{r}) - \hat{A}(\boldsymbol{r}))$ is the standard deviation of the residuals and λ is a positive number, although we would hope for them to do considerably better. They should be uniformly good across the mapped region, and display no trend in distance, latitude or longitude. However, we always expect our predictors to underperform near the boundaries of the mapped region, where they are constrained by fewer data. It is also useful to define the LOOCV score,

$$R_{\mathrm{LOO}} := \frac{1}{n}\sum_{i=1}^{n}(A_i - \hat{A}(\boldsymbol{r}_i))^2, \tag{31}$$

which should be small compared to, say, the mean variance of the elements of $\boldsymbol{A}$. Since we are unable to validate the BLUP of the density of the ISM in this way, we will take validation of $\hat{A}(\boldsymbol{r})$ to be validation of $\hat{\rho}(\boldsymbol{r})$.

3.3 Choosing the model parameters

We have observed that for a given autocovariance function, our model of the mean of the extinction has a single free parameter, μ_ρ. However, we do not in practice know the values of the parameter tuple that specifies the power spectrum, and hence the autocovariance function. We will assume that $\gamma = 11/3$ (to ensure Kolmogorov turbulence in the inertial regime), and that $\Omega = 1$ (arbitrarily). However the variance of the density, $\sigma^2_{\Delta\rho}$, and the length scale, L_0, are less certain. We might wish to find their maximum-likelihood estimate. But this would require us to assume a model for the distribution of the extinction, contrary to the assumptions of the BLUP, so that by doing this we would lose one of the principal benefits of the method. Moreover, in computing the BLUP of the extinction we are necessarily computing the GLS estimator of the mean, and we do not want a second estimate of it. Instead, we may follow a procedure much used in machine learning, and choose the pair $\sigma^2_{\Delta\rho}$ and L_0 so as to minimize the LOOCV score, R_{LOO} (equation 31). This does not allow us to formally estimate the parameter tuple in the way the method of maximum likelihood does. We should, instead, see it as a way of tuning the predictor so that it passes validation. Ultimately, our trust in the BLUP is justified only by its performance in validation, and we may choose the power spectrum's parameter tuple arbitrarily, so long as the resulting predictors pass this test.

3.4 Computational expense

The memory requirements for computing the BLUP are dominated by the storage of square matrices of size $n \times n$ and are therefore of order $O(n^2)$. The computational complexity is dominated by the inversion of the covariance matrix, $\mathbf{\Sigma}$. For small data sets, like those needed to map the dust in Orion A, we may do this using Cholesky decomposition, which has computational complexity of order $O(n^3)$. However, for significantly larger data sets, like those needed to create global dust maps, this complexity is prohibitive. Such scaling problems are common to all three-dimensional dust mapping methods and a number of solutions are available. In our case it is best to use a low-rank or sparse approximation to the covariance matrix or to use the iterative inversion method described by Wang et al. (2019), which has complexity of order $O(n^2)$. We will pursue this in future work.

4 METHODOLOGICAL TESTS USING SYNTHETIC DATA

We will shortly use our method to map dust within Orion A and its environment. In fact, we will follow Rezaei Kh et al. (2020) and Rezaei Kh. & Kainulainen (2022) by mapping the region $s/\mathrm{pc} \in [0, 500]$, $l/\mathrm{deg} \in [205, 216]$, $b/\mathrm{deg} \in [-21, -15]$, which contains approximately 10 000 stars. We will do this using two data sets: first, extinctions computed using the RJCE method; and second, extinctions reported by the StarHorse catalogue. But before doing so we will test our method using synthetic data that mimic those generated by the RJCE method.

To generate our synthetic data we realize the density field, ρ, on a $501 \times 101 \times 45$ regular lattice in s, l, and b, under the assumption that ρ is a stationary and isotropic lognormal random process having a Kolmogorov-like power spectrum (equation 9) with mean $\mu_\rho = 1 \times 10^{-3}$ mag pc^{-1}, variance $\sigma^2_{\Delta\rho} = 1 \times 10^{-6}$ mag^2 pc^{-2}, energy-injection scale $L_0 = 100$ pc, and power-law indices $\Omega = 1$ and $\gamma = 11/3$.[6] To do this, we note that the expectation and covariance of $\ln(\rho(\boldsymbol{r}))$ are given by the well-known formulae (see e.g. Coles & Barrow 1987)

$$\langle \ln(\rho(\boldsymbol{r}))\rangle = \ln(\langle \rho(\boldsymbol{r})\rangle) - \frac{1}{2}\,\mathrm{var}(\ln(\rho(\boldsymbol{r}))) \tag{32}$$

and

$$\mathrm{cov}(\ln(\rho(\boldsymbol{r}_i)), \ln(\rho(\boldsymbol{r}_j))) = \ln\left(\frac{\mathrm{cov}(\rho(\boldsymbol{r}_i), \rho(\boldsymbol{r}_j))}{\langle \rho(\boldsymbol{r}_i)\rangle\, \langle \rho(\boldsymbol{r}_j)\rangle} + 1\right) \tag{33}$$

and generate a realization of a Gaussian random process, $\ln(\rho)$, which we then exponentiate, to give ρ. We then generate a realization of A on the same $501 \times 101 \times 51$ lattice by approximating the line-of-sight integral using the trapezium rule, and choose a uniformly distributed random sample of this realization, size $n = 10\,000$, to which we add normally distributed noise with zero mean and standard deviation of 0.1 mag. This forms a set of of synthetic observations, $\boldsymbol{A} = (A_1, \ldots, A_n)$ at locations $\boldsymbol{r}_1, \ldots, \boldsymbol{r}_n$ where we work in Galactic coordinates such that $\boldsymbol{r}_i = (s_i, l_i, b_i)$. To each distance we add normally distributed noise with zero mean and standard deviation of 5 per cent. We then propagate errors from distance to extinction under the assumption that the linear approximation holds (Section

---

[6] The density field is then sampled at 1 pc intervals in s and 0.5 deg intervals in l and b.

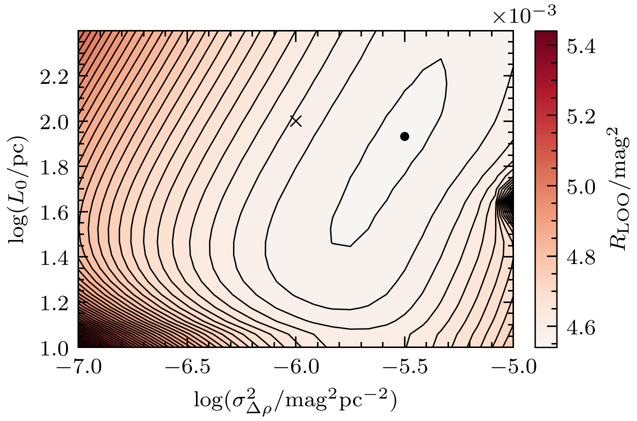

Figure 1. Recovery of the parameters of the autocovariance function for the case of synthetic data. The parameters of the autocovariance function, $\sigma^2_{\Delta\rho}$ and L_0 (equations 9 and 5), may be chosen so as to minimize the LOOCV score, $R_{\rm LOO}$ (equation 31). Here, a minimum in $R_{\rm LOO}$ is found for $\sigma^2_{\Delta\rho} = 3.0 \times 10^{-6}$ mag^2 pc^{-2} and $L_0 = 98$ pc. The true values of the parameters are $\sigma^2_{\Delta\rho} = 1 \times 10^{-6}$ mag^2 pc^{-2} and $L_0 = 100$ pc. (See Section 4 for discussion.)

3.1.1). Since the mean and maximum errors on distances are 19 and 25 pc respectively this approximation holds marginally.

We now map the entire area by evaluating $\hat{A}$ and $\hat{\rho}$ for all points on the lattice. To do this, we assume that $\Omega = 1$ and $\gamma = 11/3$, but optimize our choice of the remaining autocovariance parameters, $\sigma^2_{\Delta\rho}$ and L_0, by minimizing the LOOCV score, $R_{\rm LOO}$ (Section 3.3). This is expensive, since it involves the inversion of the matrix $\boldsymbol{\Sigma}$ for every trial parameter pair. We therefore sample $R_{\rm LOO}$ on a 25 × 25 logarithmically spaced rectangular lattice covering the region $\sigma^2_{\Delta\rho}/$ mag^2 pc$^{-2} \in [10^{-8}, 10^{-4}]$ and $L_0/{\rm pc} \in [10, 250]$. Doing this, we find that $\sigma^2_{\Delta\rho} = 3.0 \times 10^{-6}$ mag^2 pc^{-2} and $L_0 = 98$ pc (Fig. 1). These are close to the true values but we may not say they are consistent with the true values in any formal sense since we have no confidence region for them.

We then perform LOOCV (Section 3.2) by inspecting the standardized leave-one-out residuals (Fig. 2). These have approximately unit standard deviation, and exhibit no trends in s, l, or b. Accordingly, we say that our predictors pass validation. Immediately, we find that the generalized least squares estimate of the density is $\hat{\mu}_\rho = 1.2 \times 10^{-3}$ mag pc^{-1} with root mean square error (RMSE) 3.36×10^{-4} mag pc^{-1} (Appendix B), consistent with the true value of 1×10^{-3} mag pc^{-1}.

In Figs 3–6 we show our predictions for the plane $b = 3.5$ deg, and in Fig. 7 our predictions for the line of sight $l = 7$ deg, $b = 3.5$ deg. Note that we cannot expect the BLUP to reproduce features on scales smaller than the mean stellar separation. However, it is large fluctuations in the density on this interstellar scale that result in the largest increases in extinction. These largest density fluctuations cannot be probed, and as a result the density map is smoothed out. None the less, the predictions for extinction and density are everywhere consistent with their true values. Note that $\hat{A}$ is increasing in s, even though we do not constrain it to be. Similarly, note that $\hat{\rho}$ is non-negative for all $\boldsymbol{r}$. These facts are most clearly seen in Fig. 7. The prediction interval for extinction increases with distance and is inhomogeneous, just as the extinction is. The prediction interval for density does not increase with distance and is homogeneous, just as the density itself is. Note that predictions are even good close to the boundary, and in particular within the region for which $s < 200$ pc, where the predictor is most poorly constrained.

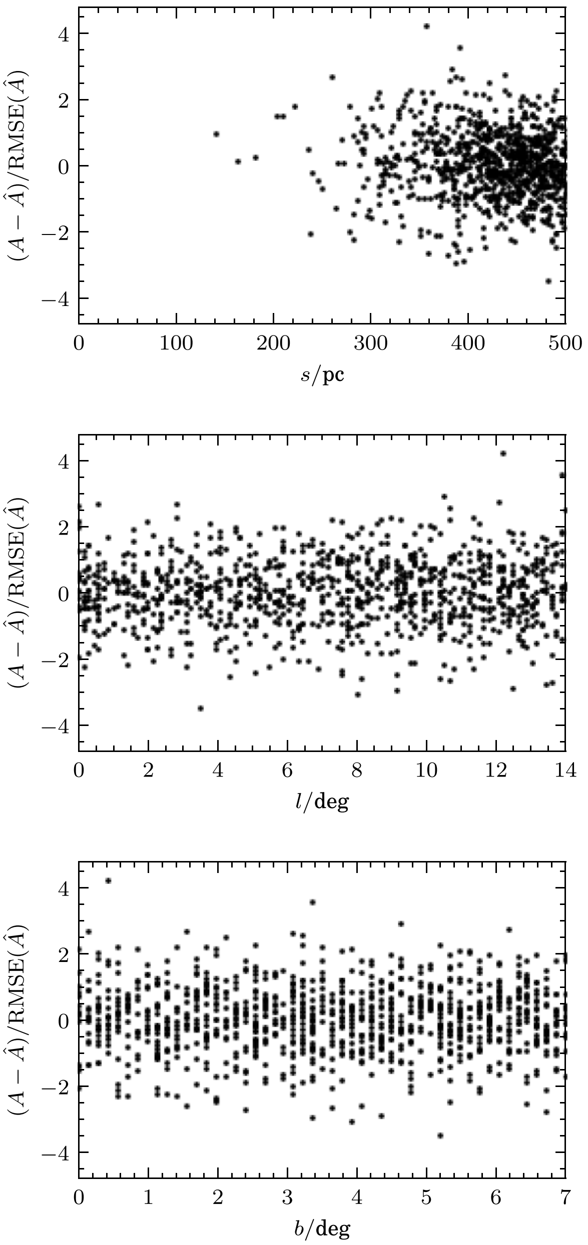

Figure 2. Validation of the best linear predictor for the case of synthetic data. The standardized leave-one-out residuals of the predicted extinction may be used to validate our maps. Here, these standardized residuals are seen to have approximately unit standard deviation, and exhibit no trends in s, l, or b. Our maps therefore pass validation. (For the sake of clarity these plots show a sample of size 1000, uniformly distributed in volume.) (See Section 4 for discussion.)

5 MAPPING DUST IN ORION A

Having tested our map-making method in this way we can now use it to create maps using each of our two data sets.

5.1 Application to colour-excess and *Gaia* data

For our RJCE data we use the catalogue compiled by Rezaei Kh. & Kainulainen (2022).[7] This was generated using H-band observations

---

[7] This catalogue is not publically available. We would like to thank Sara Rezaei Kh. for her generosity in making it available to us.

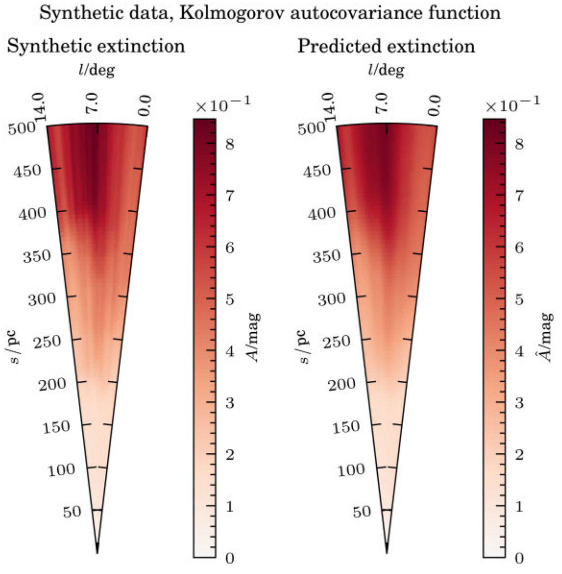

Figure 3. Our synthetic extinction field, A (left), and the field recovered from a noisy sample of it using our method, $\hat{A}$ (right), in the plane $b = 3.5$ deg. (See Section 4 for discussion.)

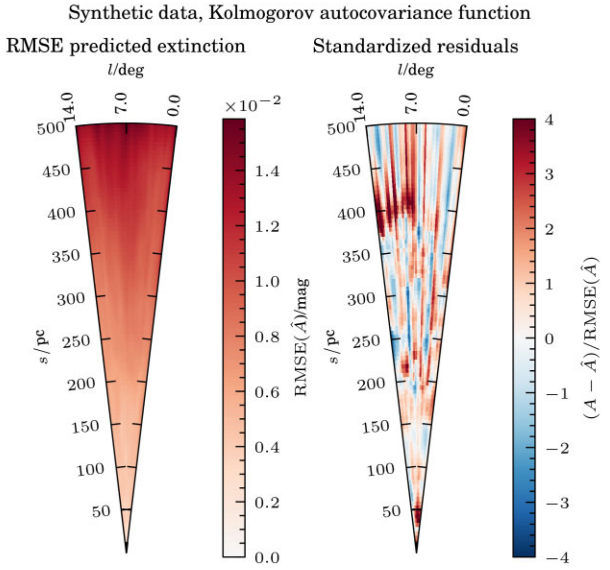

Figure 4. Synthetic data: RMSE, $\mathrm{RMSE}(\hat{A}) = \mathrm{std}(A - \hat{A})$, and standardized residuals of the predicted extinction for the plane $b = 3.5$ deg. (See Section 4 for discussion.)

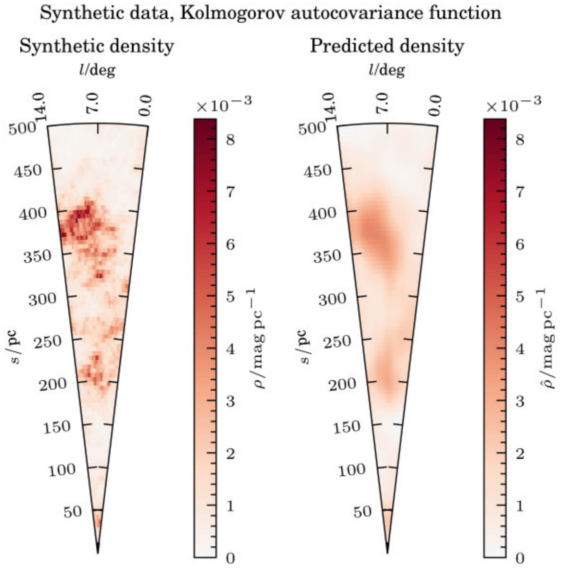

Figure 5. Our synthetic density field, ρ (left), and the field recovered from a sample of the extinction using our method, $\hat{\rho}$ (right), in the plane $b = 3.5$ deg. (See Section 4 for discussion.)

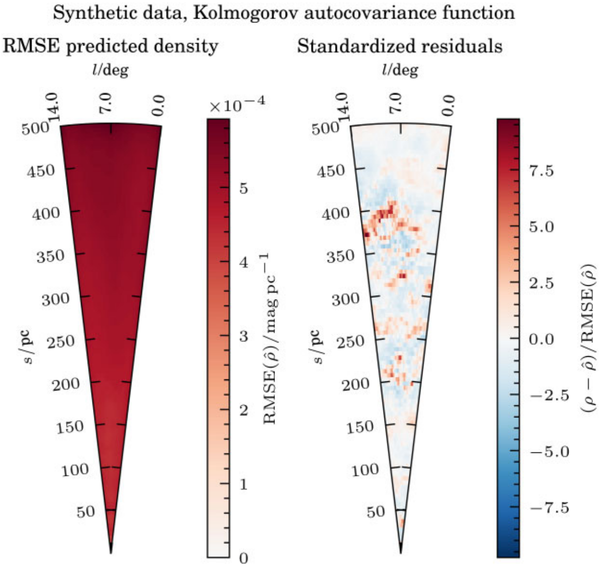

Figure 6. Synthetic data: RMSE, $\mathrm{RMSE}(\hat{\rho}) = \mathrm{std}(\rho - \hat{\rho})$, and standardized residuals of the predicted density for the plane $b = 3.5$ deg. (See Section 4 for discussion.)

from 2MASS (Skrutskie et al. 2006) and [4.5 μ]-band (i.e. W2-band) observations from WISE (Wright et al. 2010), these catalogues having been cross-matched using the algorithm provided by the *Gaia* Archive. The resulting sample was then cleaned of large-extinction outliers by eliminating all sources lying below the main-sequence in the dereddened colour-magnitude diagram (see Rezaei Kh et al. 2018, for details). These large extinctions are either artefacts resulting from the combining of two catalogues, or are associated with young stellar objects and are hence due to dusty circumstellar discs and envelopes, not to the ISM itself. We account for the errors in H and [4.5 μ], which we denote σ_H and $\sigma_{[4.5\,\mu]}$, by adding them in quadrature, so that the variance in A_{K_s} becomes $0.918^2\sigma_H^2 + 0.918^2\sigma_{[4.5\,\mu]}^2 + 0.1^2$ mag^2. The resulting mean error in extinction is 0.17 mag, and the standard deviation of the error in extinction is 0.073 mag.

We combine these extinction data with the line-of-sight distances inferred by Bailer-Jones et al. (2021) using *Gaia* EDR3 (Gaia Collaboration 2016, 2021), again using the *Gaia* Archive cross-matching algorithm. We take for our distance prediction the median of the posterior distribution (which we expect to be close to the mean of the predicted distance since the PDFs are unimodal and approximately symmetric at such small distances), and for our error half the difference of the 0.16 and 0.84 quantiles. The mean error in distance is 6.3 pc, and the standard deviation of the error in distance is 11 pc. We propagate errors from distance to extinction under the assumption that the linear approximation holds (Section 3.1.1).

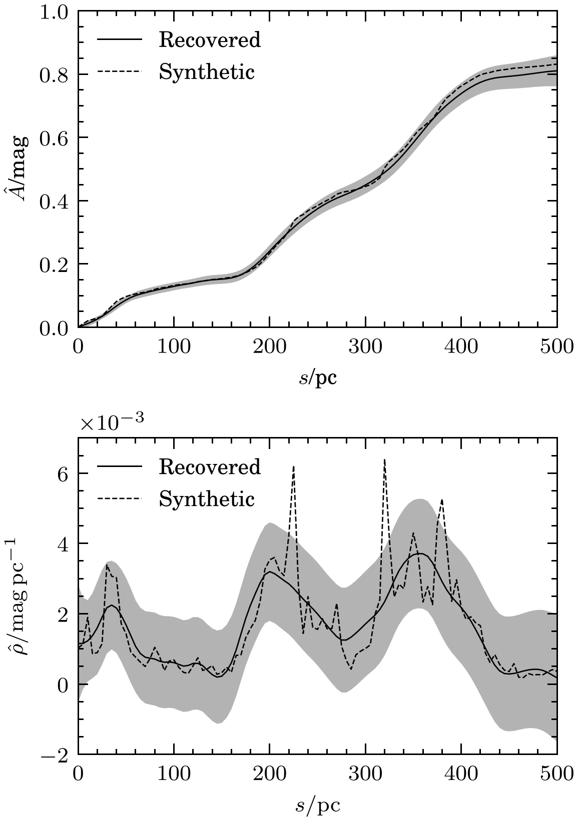

Figure 7. Our synthetic fields A (top) and ρ (bottom), along with the fields recovered using our method, along the line of sight $l = 7$ deg, $b = 3.5$ deg. In each case the synthetic field is shown as a dashed line, the recovered field is shown as a solid line, and the three-RMSE prediction interval shown as a shaded band. (See Section 4 for discussion.)

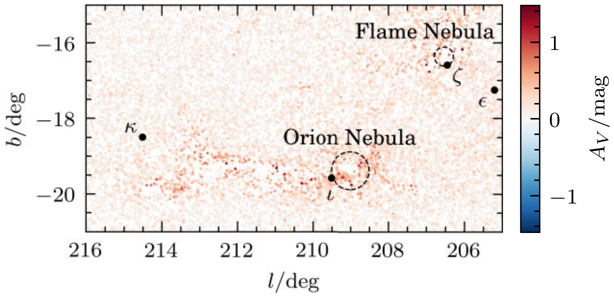

Figure 8. The $K_{\rm s}$-band extinctions, computed using the RJCE method, for stars in the direction of the giant molecular cloud Orion A (note that the RJCE method permits unphysical negative extinctions). The principal stars of the Orion constellation (ϵ Ori, ζ Ori, κ Ori, ι Ori) are marked. The head of Orion A is coincident with the Orion Nebula. Its tail extends south west (parallel to the Galactic plane) for several degrees, and is evident from the lack of observations in this region (due to high extinctions). The south-west extremity of the giant molecular cloud Orion B is coincident with the Flame Nebula. It extends north-west (perpendicular to the Galactic plane) for several degrees, beyond the extent of the figure. It too is evident from a lack of observations.

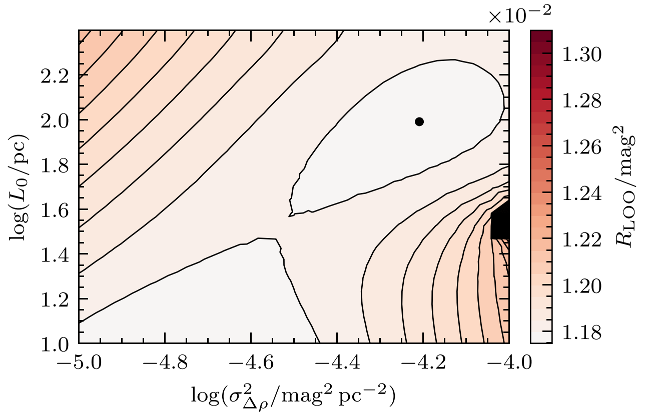

Figure 9. Recovery of the parameters of the autocovariance function for the case of RJCE and *Gaia* data. The LOOCV, $R_{\rm LOO}$, is found to have a minimum for $\sigma^2_{\Delta\rho} = 6.2\times10^{-5}$ mag^2 pc^{-2} and $L_0 = 98$ pc. Contours are shown at intervals of 5×10^{-5} mag^2. (See Section 5 for discussion.)

The final sample contains 10 180 stars, having an average stellar separation of 3.9 pc. Of these sources, 1 434 have negative measured extinctions. We show all extinctions in Fig. 8.

We again map the entire region by evaluating $\hat{A}$ and $\hat{\rho}$ at all points on a $501\times501\times45$ regular lattice in s, l, and b, repeating the analysis we performed using synthetic data. By minimizing the LOOCV score, $R_{\rm LOO}$, we find that that $\sigma^2_{\Delta\rho} = 6.2\times10^{-5}$ mag^2 pc^{-2} and $L_0 = 98$ pc (Fig. 9). (Note that the precision of these values is limited by the size of the grid we use to search parameter space.) The leave-one-out residuals have better than unit standard deviation, and again exhibit no trends in s, l, or b, so that we may again say that our predictors pass validation (Fig. C1). The GLS estimate of the density is $\hat{\mu}_\rho = 3.8\times10^{-4}$ mag pc^{-1} with RMSE 2.75×10^{-3} mag pc^{-1}(see Appendix B for a discussion of our quoted errors). In Figs 10 and 11 we show our predictions for the plane $b = -19.5$ deg (corresponding to fig. 4 in the paper by Großschedl et al. 2019), and in Fig. 12 we show our predictions for a sequence of on-sky regions at increasing line-of-sight distances (corresponding to figs 2 and 5 in the 2020 paper by Rezaei Kh et al.). Note that $\hat{A}$ is not increasing in s, and that $\hat{\rho}$ is negative for some $\boldsymbol{r}$. Nevertheless, prediction intervals for $\hat{A}$ are consistent with its being increasing in s, and prediction intervals for $\hat{\rho}$ are consistent with its being non-negative for all $\boldsymbol{r}$.

Our maps clearly identify the head of Orion A (at $s = 390$ pc, $l = -19.5$ deg, $b = 209$ deg) and its tail, which extends to a distance of $s = 470$ pc albeit varying in density along its length. They also clearly identify the foreground cloud first noted by Rezaei Kh et al. (2020). In the plane $b = -19.5$ deg (Fig. 11) this appears as a chevron, the apex of which is located at $s = 350$ pc, $l = 210$ deg. In the plane $s = 345$ pc (Fig. 12) it is seen to have two lobes, one centred at $l = -19.5$ deg, $b = 211$ deg, and the other centred at $l = 206.5$ deg, $b = 17$ deg. The lower of these is located at the apex of the chevron, and is bifurcated at smaller distances. Fig. 13 shows our predictions for the lines of sight centred on these lobes (corresponding to fig. 3 in the 2020 paper by Rezaei Kh et al.).

Let us consider possible systematic errors in our predictions. These might arise from inadequate models of the mean and covariance of the extinction field (equations 14 and 15) or from systematic errors in the distance and extinction data that we use. Such errors might be associated with stars of a particular spectral class, causing them to appear too close or too distant, too red or too blue. The distances to our sources have been inferred using only parallax information so we do not expect there to be any systematic errors of this type in distance. However, the RJCE method for computing extinctions relies on a linear fit to observed colours. This assumption of linearity is good for a large range of spectral classes but could result in the extinctions of very cool stars being underestimated and the extinctions of very

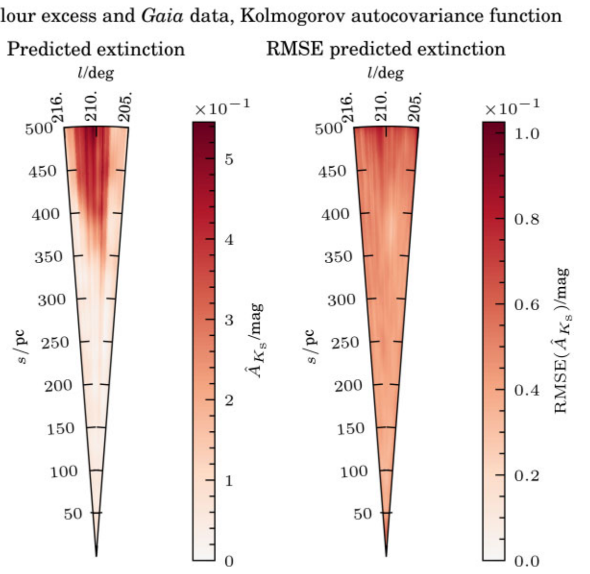

Figure 10. Colour excess and *Gaia* data: Predicted extinction, $\hat{A}_{K_s}$ (left), and its RMSEs, RMSE($\hat{A}_{K_s}$) (right), for the plane $b = -19.5$ deg. (See Section 5 for discussion.)

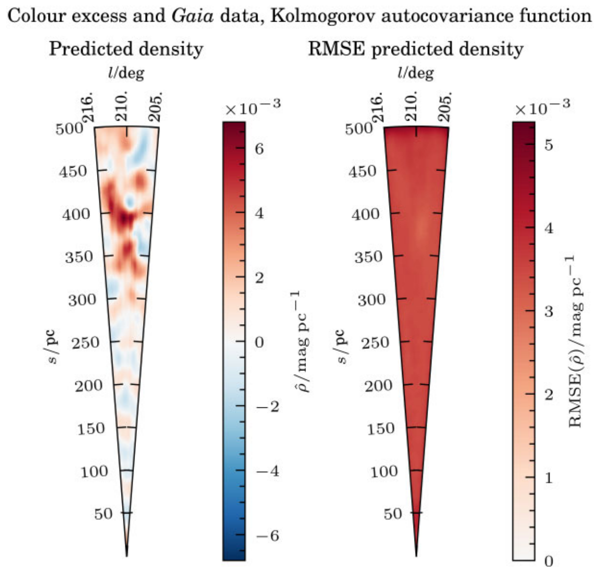

Figure 11. Colour excess and *Gaia* data: Predicted density, $\hat{\rho}$ (left), and its RMSEs, RMSE($\hat{\rho}$) (right), for the plane $b = -19.5$ deg. The head of Orion A is seen at $s = 390$ pc and a foreground cloud at $s = 350$ pc. (See Section 5 for discussion.)

hot stars being be overestimated. Systematic errors associated with spectral class should appear as overdensities in the joint distribution of (i) spectral class and distance or (ii) spectral class and extinction, and such overdensities should alert us to the presence of systematic errors in the computed values of either quantity. We can use the dereddened colour $(G - K_s)_0$ (computed using using the exinction law of Cardelli, Clayton & Mathis 1989) as a proxy for spectral class and inspect the histogram for each distribution (not shown). In neither case do we see overdensities associated with any particular value of colour. We therefore claim that our data are free of significant systematic errors relating to spectral class.

5.2 Application to StarHorse data

The StarHorse catalogue includes quantiles for the inferred PDFs of a source's extinction and distance, and therefore neatly provides all the information we need to construct a dust map. We use the first StarHorse catalogue (Anders et al. 2019) rather than the second (Anders et al. 2021) since this second catalogue begs the question by assuming for a prior on extinction the maps of Green et al. and Drimmel, Cabrera-Lavers & López-Corredoira. Each source in the StarHorse catalogue is associated with the compound flags `SH_GAIAFLAG`, which quantifies the quality of the *Gaia* astrometry and photometry used, and `SH_OUTFLAG`, which quantifies the quality of StarHorse's inferences (Anders et al. 2019). The `SH_GAIAFLAG` flag consists of three digits flagging (1) high renormalized unit weight error, warning of a spurious astrometric solution, (2) high colour excess factor, warning of spurious photometry, and (3) source variability. The `SH_OUTFLAG` flag consists of five digits flagging (1) overall unreliability, warning of physically inconsistent inferred stellar properties, (2) large distance, warning

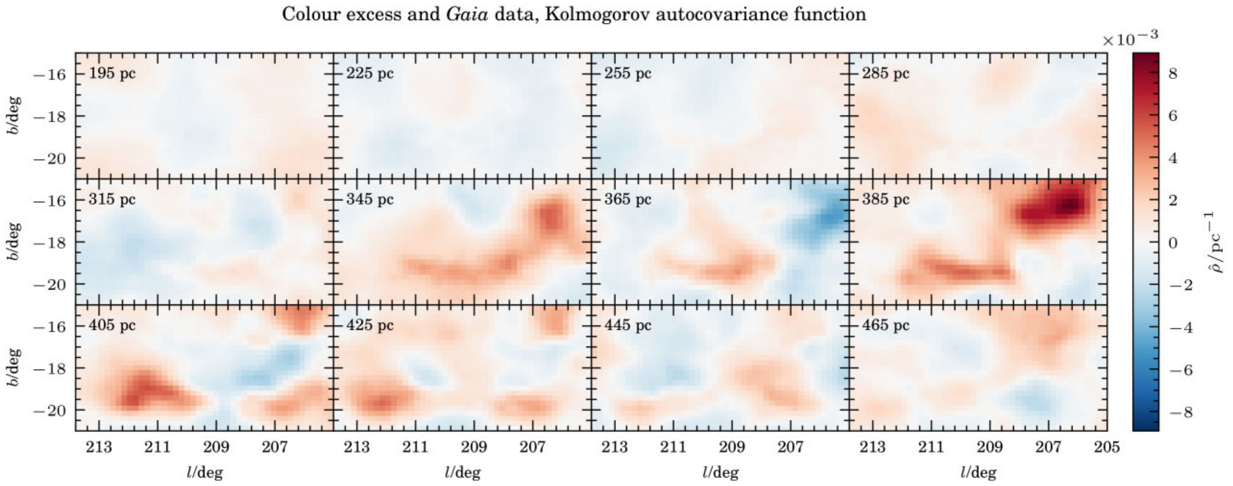

Figure 12. Colour excess and *Gaia* data: Predicted density, $\hat{\rho}$, for a series of line-of-sight distances, s, evaluated on a regular lattice with spacing of 0.5 deg. This figure matches fig. 2 in the paper by Rezaei Kh et al. (2020). The head of Orion A is seen in panels $s = 385$ pc and $s = 405$ pc. A foreground cloud is seen in the panel $s = 345$ pc. (See Section 5 for discussion.)

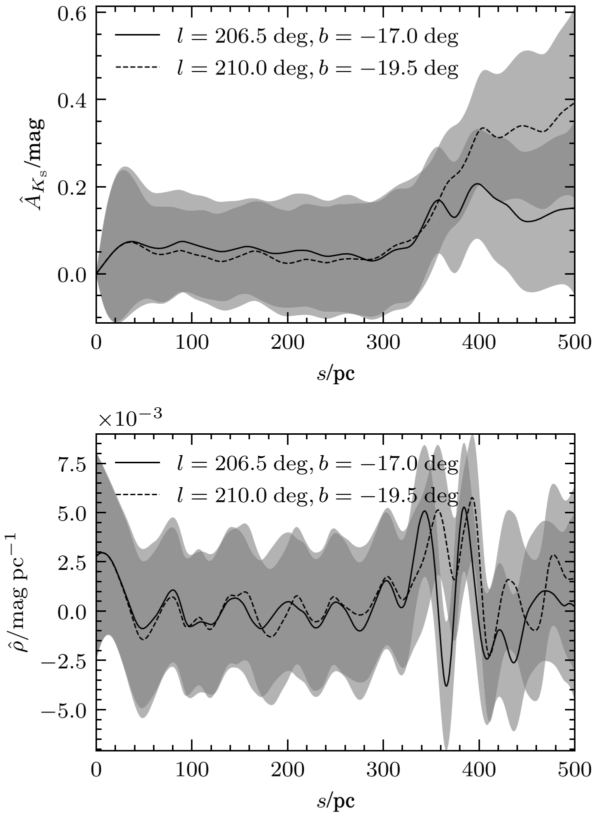

Figure 13. Colour excess and *Gaia* data: Extinction, A_{K_s} (top), density, ρ (bottom), and their predicted values, $\hat{A}_{K_s}$ and $\hat{\rho}$, for the lines of sight $l = 206.5$ deg, $b = -17$ deg and $l = 210$ deg, $b = -19.5$ deg. These pass through the two lobes of the foreground cloud. The three-RMSE prediction intervals are shown as shaded bands. (See Section 5 for discussion.)

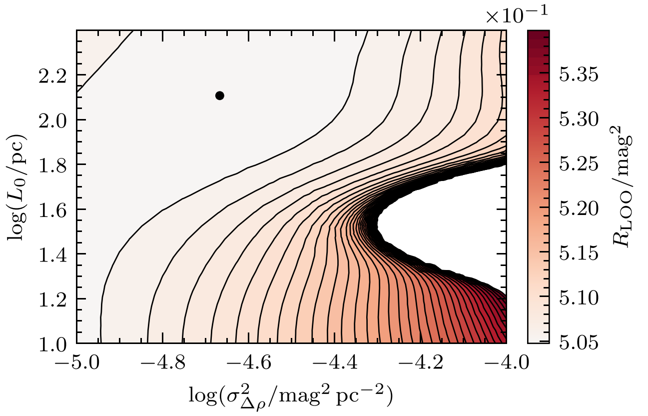

Figure 14. Recovery of the parameters of the autocovariance function for the case of StarHorse data. The LOOCV score, R_{LOO}, is found to have a minimum for $\sigma^2_{\Delta\rho} = 2.2 \times 10^{-5}$ mag^2 pc^{-2} and $L_0 = 128$ pc. The covariance matrix, $\mathbf{\Sigma}$, is nearly singular for some parameter combinations (region shown blank) , meaning that R_{LOO} cannot be computed. Contours are shown at intervals of 1×10^{-3} mag^2. (See Section 5 for discussion.)

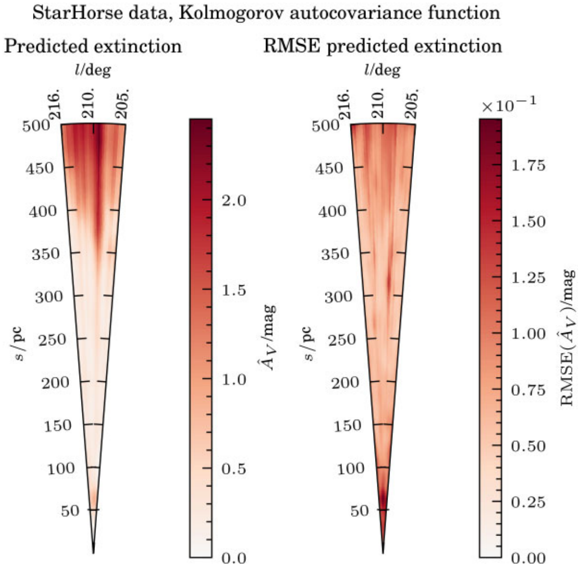

Figure 15. StarHorse data: Predicted extinction, $\hat{A}_V$ (left), and its RMSEs, RMSE($\hat{A}_V$) (right), for the plane $b = -19.5$ deg. Cp. Fig. 15. (See Section 5 for discussion.)

of a spuriously large inferred distance, (3) unreliable extinction, warning of a spuriously small or spuriously large inferred extinction, (4) large extinction uncertainty, warning of an inferred extinction uncertainty of unit magnitude or greater, and (5) small uncertainty, warning of spuriously small uncertainties in any inferred stellar property. We use sources for which `SH_GAIAFLAG` is `000` and `SH_OUTFLAG` is `00000`, ensuring that potentially spurious statistics of each kind are not included in our sample.

For each source in this sample, we realize a sample of the posterior extinction by assuming its PDF to be uniform within quantiles. In order to do this, we assume a lower limit on A_V of -0.3 mag, and an upper limit of 4 mag, consistent with the StarHorse prior PDF for extinctions with errors in distance greater that 20 per cent. We take the standard deviation of the posterior extinction to be half the difference of the 0.16 and 0.84 quantiles. The mean error in extinction is then 0.17 mag, and the standard deviation of the error in extinction is 0.011 mag.

We again take for our distance prediction the median of the posterior distribution, and for our error half the difference of the 0.16 and 0.84 quantiles. The mean error in distance is then 13 pc, and the standard deviation of the error in distance is 9.7 pc. Again, we propagate errors from distance to extinction under the assumption that the linear approximation holds (Section 3.1.1). The final sample contains 12 719 stars, having an average stellar separation of approximately 3.7 pc. Of these sources, 1 434 have negative extinctions.

By minimizing the LOOCV, R_{LOO}, we find that that $\sigma^2_{\Delta\rho} = 2.2 \times 10^{-5}$ mag^2 pc^{-2}, and $L_0 = 128$ pc (Fig. 14). However, the leave-one-out residuals have very high standard deviation of 4.5 mag^2, although they exhibit no trends in s, l, or b (Fig. C2). As such, they fail validation. This may be due to the presence of young stellar objects in the StarHorse catalogue, which we have made no attempt to identify and remove, and which violate the assumptions of our model. Nevertheless, we find that GLS estimate of the density is $\hat{\mu}_\rho = 6.2 \times 10^{-4}$ mag pc^{-1} with RMSE 1.94×10^{-3} mag pc^{-1} and, as before, we plot our predictions for the plane $b = -19.5$ deg (Figs 15 and 16), a sequence of on-sky regions at increasing line-of-sight distances (Fig. 17), and the lines of sight $l = 206$ deg, $b = -17$ deg, and $l = 210$ deg, $b = -19.5$ deg (Fig. 18). Note that StarHorse extinctions are given for the V-band rather than K_s-band, and that according to the Cardelli, Clayton & Mathis (1989) extinction law,

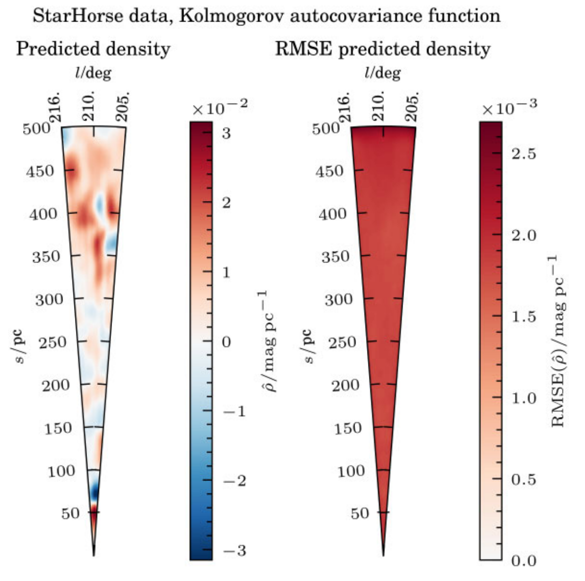

Figure 16. StarHorse data: Predicted density, $\hat{\rho}$ (left), and its RMSEs, RMSE($\hat{\rho}$) (right), for the plane $b = -19.5$ deg. Cp. Fig. 11. (See Section 5 for discussion.)

$A_V/A_{K_s} = 8.8$. Again, we note that $\hat{A}$ is not increasing in s, and $\hat{\rho}$ is negative for some $\boldsymbol{r}$. Nevertheless, prediction intervals for $\hat{A}$ are again consistent with its being increasing in s, and prediction intervals for $\hat{\rho}$ are again consistent with its being non-negative for all $\boldsymbol{r}$.

The head of Orion A (at $s = 390$ pc, $l = 209$ deg, $b = -19.5$ deg) appears only faintly in our maps, although the tail and foreground cloud both appear clearly. In the plane $b = -19.5$ deg the foreground cloud is seen as a linear structure rather than chevron, though it is again seen to have two lobes in the plane $s = 345$ pc. Since these maps do not pass validation we do not use them to make comment on the distribution of dust in Orion A. In particular we do not use them to comment on the existence of a foreground cloud.

Here we have used a single realization of the StarHorse posterior extinctions. Alternative realizations of the posterior extinctions produce similar results. We could instead have made multiple realizations and generated an empirical distribution for the predictor $\hat{A}(\boldsymbol{r})$. In practice, however, we find that the mean and standard deviation of the empirical distribution converge quickly, and that they are in fact well approximated by a single sample.

6 DISCUSSION

To make our maps we have used a physically motivated Kolmogorov-like autocovariance function to describe the density fluctuations of the ISM. When using the BLUP (equation 20) it is common to use one of many off-the-shelf library functions that do not have direct physical motivation. For example, it is very common to use a powered-exponential autocovariance function, $k_{\rm PE}$, given by

$$k_{\rm PE}(\delta) = \sigma^2_{\rm PE}\exp\left(-\left(\frac{\delta}{L_{\rm PE}}\right)^{\alpha}\right) \tag{34}$$

where $\sigma^2_{\rm PE}$ is the variance of the field, $L_{\rm PE}$ is a characteristic length scale, and where $\alpha \in (0, 2]$. Particularly popular is the case of $\alpha = 2$, when $k_{\rm PE}$ is known as the 'squared-exponential autocovariance function'. Autocovariance functions with compact support are also attractive, since they reduce the computational burden of computing and inverting the covariance matrix, $\boldsymbol{\Sigma}$. Indeed Rezaei Kh et al. (2017) recommended the use of compactly supported functions for dust mapping, and in their work use Gneiting's function, $k_{\rm G}$ (Gneiting 2002), given by

$$k_{\rm G}(\delta) = \sigma^2_{\rm G}\left(1+\left(\frac{\delta}{L_{\rm G}}\right)\right)^{-3}\left(\left(1-\frac{\delta}{L_{\rm G}}\right)\cos\left(\frac{\pi\delta}{L_{\rm G}}\right) + \frac{1}{\pi}\sin\left(\frac{\pi\delta}{L_{\rm G}}\right)\right) \tag{35}$$

if $\delta/L_{\rm G} \in [0, 1]$, and $k_{\rm G}(\delta) = 0$ otherwise, where $\sigma^2_{\rm G}$ is the variance of the field and $L_{\rm G}$ is a characteristic length scale for the field, above which the autocovariance vanishes.

Any such standard autocovariance function may be used with our method by integrating it to give an approximation to $\mathrm{cov}(A(\boldsymbol{r}_i), A(\boldsymbol{r}_j))$ according to equation (5). In turn, we can approximate the functions f and g (equations 16 and 17). (See Appendix B for plots of these approximations.) Although library functions of this kind have no direct physical motivation, we do require them to have properties consistent with the physics of the ISM. In particular we require the random processes they define to be continuous, undifferentiable and to have physically meaningful characteristic length scales. We should be mindful of these properties when we specify the autocovariance function and when we interpret our predictions. A stationary and isotropic random field is continuous (in the mean square) if its autocovariance function is continuous at zero, and is differentiable (in the mean square) if its autocovariance function is also twice differentiable at zero (i.e. a stationary random field is m-times differentiable everywhere if its autocovariance function is $2m$-times differentiable at zero). The Kolmogorov-like autocovariance function is undifferentiable at zero, and hence defines an undifferentiable random field. This roughness is clear in our synthetic dust maps (bottom panel of Fig. 7). Gneiting's function is also undifferentiable at zero, and therefore also defines an undifferentiable random field. The powered-exponential is differentiable only for $\alpha = 2$, when it is infinitely differentiable, and hence defines an infinitely differentiable random field. For $\alpha \neq 2$, however, it is undifferentiable, and hence again defines an undifferentiable random field. Indeed, realizations of the random field increase in roughness as α decreases. Whereas Gneiting's function is suitable for specifying the dust's autocovariance, the squared-exponential kernel is not. Using it will result in maps that lack sharpness and exhibit features that are ill-defined.

To find a physically meaningful interpretation of the characteristic length scale we may use the *integral length scale* of a random field, which is much used in the study of turbulence (Tennekes 1972). Suppose that k is a autocovariance function with variance σ^2 and characteristic length scale L. The integral length scale of the stationary random field associated with k is[8]

$$l(k) = \frac{1}{\sigma^2}\int_0^\infty |k(\delta)|\,\mathrm{d}\delta. \tag{36}$$

In order to make explicit its dependence on σ^2 and L let us write k as $k(\cdot\,; \sigma^2, L)$. We introduce the *physical length scale*, Λ, such that

$$\frac{1}{\sigma^2}\int_0^\infty |k(\delta; \sigma^2, L)|\,\mathrm{d}\delta = \frac{1}{\sigma^2_{\Delta\rho}}\int_0^\infty |k_{\Delta\rho}(\delta; \sigma^2_{\Delta\rho}, \Lambda)|\,\mathrm{d}\delta, \tag{37}$$

noting that, whereas k is the autocovariance function of interest, $k_{\Delta\rho}$ is the autocovariance of the density fluctuations (equation 8) with

---

[8] Note that this integral always exists since k is absolutely integrable.

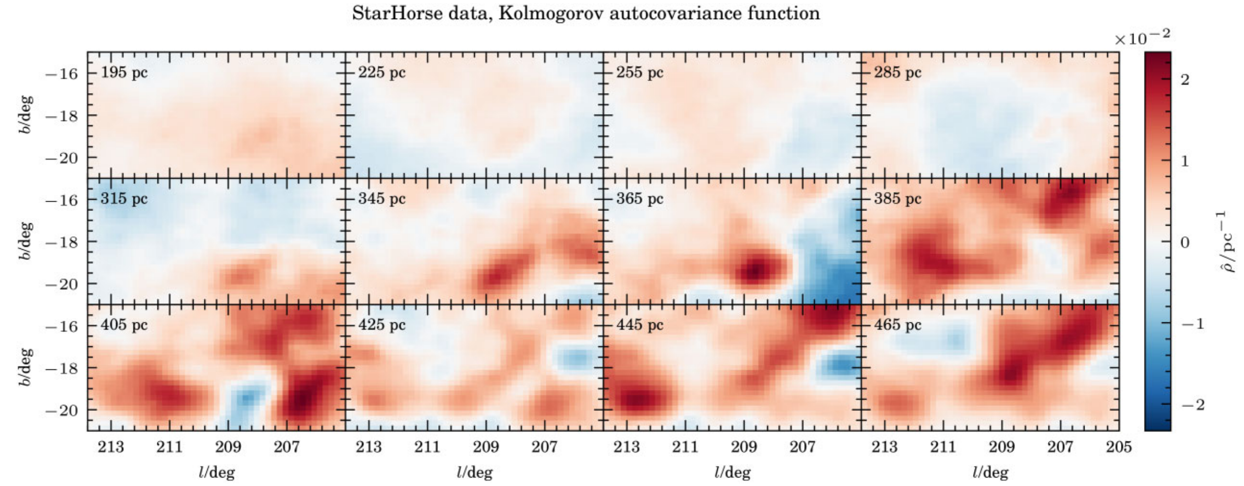

Figure 17. StarHorse data: Predicted density, $\hat{\rho}$, for a series of line-of-sight distances, s. Cp. Fig. 12. (See Section 5 for discussion.)

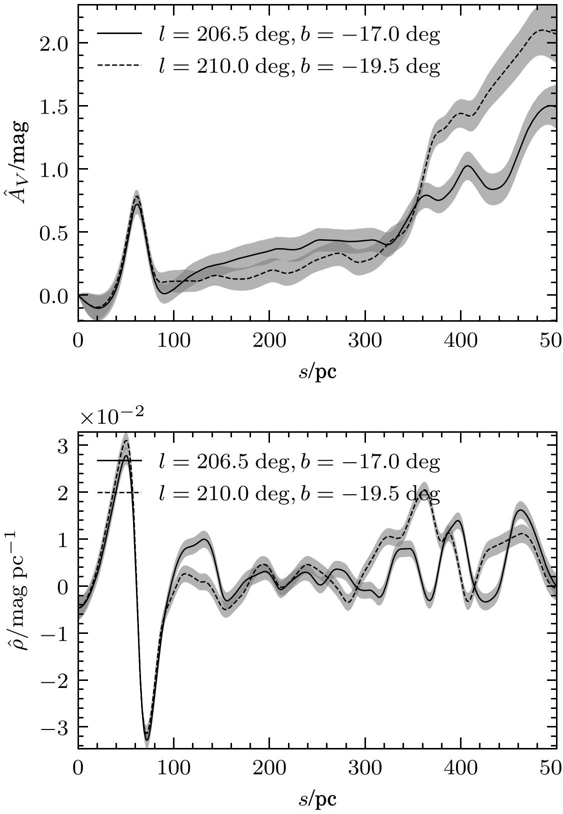

Figure 18. StarHorse data: Extinction, A_V (top), density, ρ (bottom), and their predicted values, $\hat{A}_V$ and $\hat{\rho}$, for the lines of sight $l = 206.5$ deg, $b = -17$ deg and $l = 210$ deg, $b = -19.5$ deg. The three-RMSE prediction intervals are shown as shaded bands. Cp. Fig. 13. (See Section 5 for discussion.)

power spectrum defined by Sale & Magorrian (2014) and given in equation (9). This may be rewritten as

$$\frac{L}{\sigma^2}\int_0^\infty |k(\delta;\sigma^2,1)|\,\mathrm{d}\delta = \frac{\Lambda}{\sigma^2_{\Delta\rho}}\int_0^\infty |k_{\Delta\rho}(\delta;\sigma^2_{\Delta\rho},1)|\,\mathrm{d}\delta, \tag{38}$$

or, equivalently,

$$\Lambda = \frac{\int_0^\infty |k(\delta;1,1)|\,\mathrm{d}\delta}{\int_0^\infty |k_{\Delta\rho}(\delta;1,1)|\,\mathrm{d}\delta} L, \tag{39}$$

which allows us to find the physical length scale associated with a given autocovariance function. It approximates the energy-injection scale of the equivalent Kolmogorov-like density field. The Kolmogorov-like, squared-exponential, and Gneiting functions have physical length scales L_0, $2.51L_{\mathrm{PE}}$, and $0.466L_{\mathrm{G}}$.

We can illustrate the consequences of our choice of autocovariance function by making maps using the squared-exponential and Gneiting functions with the data of Rezaei Kh. & Kainulainen (2022) and Bailer-Jones et al. (2021; Section 5). For the squared-exponential function we find no minimum in the LOOCV score: for large regions of parameter space inversion of $\mathbf{\Sigma}$ is numerically unstable (and hence the LOOCV may not be computed), whereas elsewhere the LOOCV score reduces monotonically as L_{PE} approaches 10 pc (the lower limit of the search region) for all values of σ^2_{PE} (Fig. 19, top panel). This reflects the fact that the autocovariance function is misspecified, and that the LOOCV score of the BLUP can only be reduced by its overfitting the data. We may none the less choose the parameters of our function arbitrarily. Suppose, then, that we choose $\sigma^2_{\mathrm{PE}} = 1 \times 10^{-5}$ mag^2 and $L_{\mathrm{PE}} = 40$ pc, such that L_{PE} is the characteristic length we would expect if $\Lambda = 100$ pc. In this case our predictors do pass validation, and we are able to make the maps shown in Figs 20 and 21. Note that the features in our map (in particular, the head and tail of Orion A, as well as the foreground cloud) are no longer resolved and that the map itself is much less sharp than before, reflecting the fact that the squared-exponential function results in smooth random fields that do not have the rough properties of the ISM, and that because of this its length scale cannot be given a physical interpretation. Moreover, our results are sensitive to our choice of length scale, meaning that a scaling of L_{PE} will result in a scaling of the predicted features. With a characteristic length scale of $L_{\mathrm{PE}} = 15$ pc our predictors again pass validation, and the features in our map are resolved, but still lack sharpness. (We do not show this effect in our figures.)

For Gneiting's function we find two minima in the LOOCV score, at $\sigma^2_{\mathrm{G}} = 1.78 \times 10^{-5}$ mag^2, $L_{\mathrm{G}} = 13.1$pc, and $\sigma^2_{\mathrm{G}} = 5.62 \times 10^{-5}$ mag^2, $L_{\mathrm{G}} = 191$pc (Fig. 19, bottom panel). Both pairs of parameters result in predictors that pass validation. However, it is the second pair that corresponds to the physical length scale we

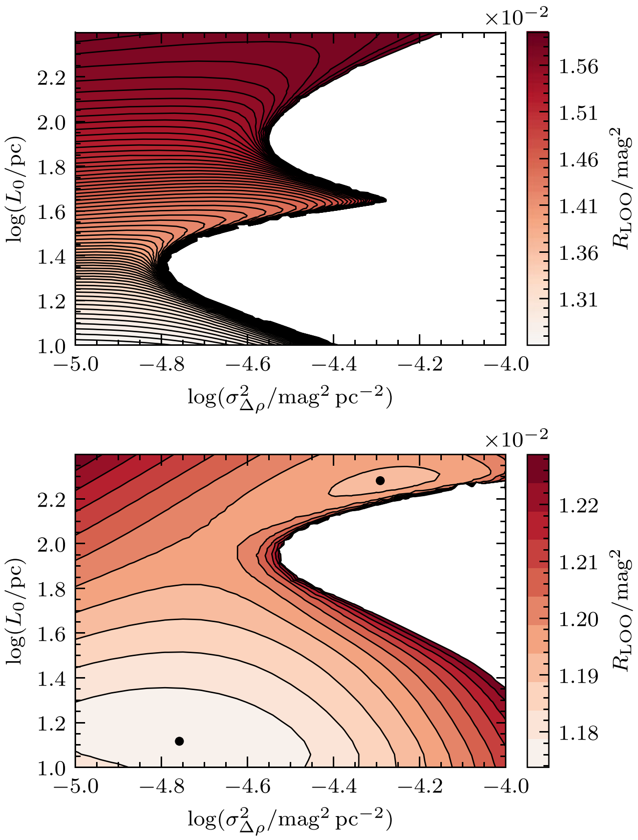

Figure 19. Top: Recovery of the parameters of squared-exponential autocovariance function (equation 34; $\alpha = 2$). The LOOCV score, R_{LOO}, is found to have no minimum. Bottom: Recovery of the parameters of Gneiting's autocovariance function (equation 35). The LOOCV score, R_{LOO}, is found to have a minimum for $\sigma^2_{\Delta\rho} = 1.78 \times 10^{-5}$ mag^2, $L_0 = 13.1$ pc and $\sigma^2_{\Delta\rho} = 5.62 \times 10^{-5}$ mag^2, $L_0 = 191$ pc. In both cases, the covariance matrix, $\mathbf{\Sigma}$, is nearly singular for some parameter combinations (region shown blank), meaning that R_{LOO} cannot be computed. (Cp. Fig. 9.) Contours are shown at intervals of 5×10^{-5} mag^2. (See Section 6 for discussion.)

expect, since in this case we find that $\Lambda = 89$ pc. Maps made using this second pair of parameters are shown in Figs 22 and 23. They are all but indistinguishable from maps made using the first pair of parameters, indicating that our predictors are somewhat robust against misspecification of the length scale. Moreover, they are very similar to the maps made using the Kolmogorov-like autocovariance function (Figs 10 and 11), indicating that Gneiting's function provides a good approximation to the Kolmogorov-like function.

7 CONCLUSION

We have made a three-dimensional dust map of the giant molecular cloud Orion A by computing the BLUP (equation 20) of the extinction at every point on an arbitrarily dense lattice using extinctions for a set of observed stars in the region of this lattice. The BLUP requires us to make very few assumptions about the statistical properties of the ISM. It requires only that we know the covariance of the density at any two points, and that we have a model of the expected value of the density at any one point. Beyond this knowledge of the first and second moments of the density, we need know nothing of its distribution.

In practice, however, we do not know the covariance of the extinctions at two points, and instead have a model of it, just as we have a model for the expected value. Since we do not know the distribution of the dust density we are not able to use the method of maximum likelihood to optimize this model, but instead fit it to the data by choosing the parameter tuple that minimizes the LOOCV score. It is also convenient to assume that the density field is stationary and isotropic, and that it is described by Kolmogorov's theory of turbulence within the inertial range set by the energy-injection and energy-dissipation scales. Moreover, by assuming that the density is isotropic and homogeneous our model of the mean density has only one free parameter, μ_ρ, which we can recover in the course of making our predictions.

This agnosticism is both a strength and a weakness of our method, since it does not allow us to encode the fact that density is always non-negative. None the less, in experiments using synthetic data we find that predicted densities are, in practice, everywhere non-negative. With observational data we find that predicted densities are, in practice, everywhere consistent with being non-negative. Negative predicted densities are the result of spuriously high predicted extinctions regressing to the mean along the line of sight, meaning that, along a line of sight, the extinction field is not monotone. Observational data also suffer from selection effects that cause the average observed extinction to decrease with distance (Sale 2015). The more heavily extinguished a star is the fainter it is and hence the less chance it has of appearing in any magnitude-limited catalogue. These negative densities are therefore due to either a lack of data or to model mispecification. In the latter case, either our assumptions about the statistics of the ISM fail to do it justice, or the data include sources with extinctions that are not due exclusively to the dust of the ISM (for example, the extinctions of young stellar objects is partially due to their dusty circumstellar discs and envelopes). Such sources are likely to be present in any catalogue, especially in catalogues containing nebulae like those of Orion A, even after cleaning.

The choice of autocovariance function is crucial to the quality of any three-dimensional dust map. We have used the physically motivated Kolmogorov-like function defined by Sale & Magorrian (2014). Other autocovariance functions may be used as substitutes so long as they have the appropriate properties, i.e. so long as they define a density field that is continuous and rough, in which case they seem to adequately describe the fractal behaviour of the ISM. These requirements exclude the popular squared-exponential autocovariance function, which defines continuous but smooth random fields. The use of a squared-exponential autocovariance function will result in smooth maps, the features of which will be washed out. Nevertheless, the Kolmogorov-like function has a physically meaningful parameter tuple that library functions like the powered exponential and the Gneiting function do not. However, by comparing the integral length scale of a substitute autocovariance function with that of the Kolmogorov-like autocovariance function we may find the physical length scale that corresponds to its characteristic length scale. This physical length scale approximates the energy-injection scale, and hence gives physical meaning to the characteristic length scale of the substitute function.

The maps we have made using RJCE extinction data combined with line-of-sight distances inferred by Bailer-Jones et al. (2021) broadly agree with those of Rezaei Kh et al. (2020) and Rezaei Kh. & Kainulainen (2022). In particular, they corroborate Rezaei Kh's claim that a foreground cloud exists at a distance of 350 kpc. However, the maps we have made using StarHorse data (Anders et al. 2019) fail even to identify the head of Orion A. Crucially, these maps fail validation, alerting us to the fact that they are untrustworthy.

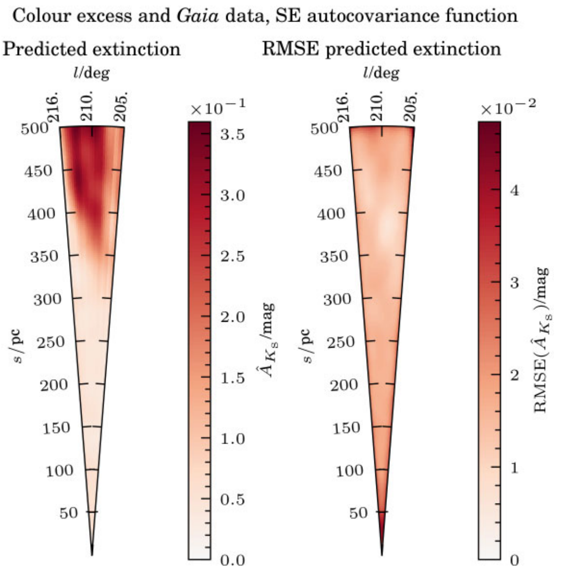

Figure 20. Colour excess and *Gaia* data: Predicted extinctions, $\hat{A}_{K_s}$, and their RMSEs, RMSE($\hat{A}_{K_s}$), computed using the squared-exponential function (equation 34), for the plane $b = -19.5$ deg. (See Section 6 for discussion. Cp. Fig. 10, which shows predictions computed using the Kolmogorov-like function.)

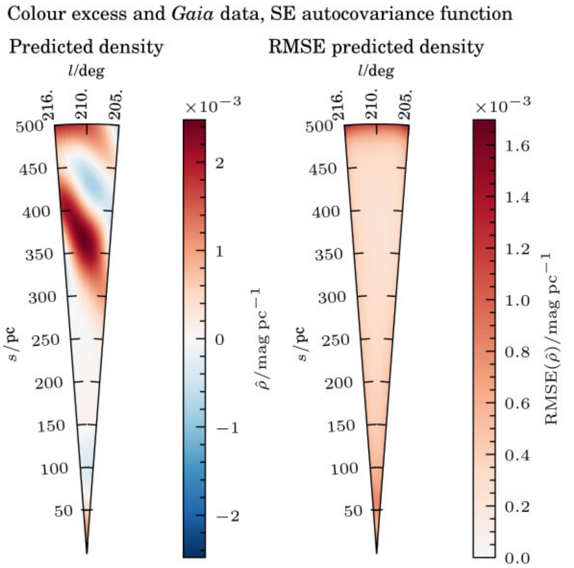

Figure 21. Colour excess and *Gaia* data: Predicted density, $\hat{\rho}$, and their RMSEs, RMSE($\hat{\rho}$), computed using the squared-exponential function (equation 34), for the plane $b = -19.5$ deg. (See Section 6 for discussion. Cp. Fig. 11, which shows predictions computed using the Kolmogorov-like function.)

The unfiltered StarHorse catalogues, though wonderful, must be used with care. They contain many sources, such as young stellar objects, that violate the assumptions of its methodology, and which therefore have spurious extinction entries that are not flagged as such.

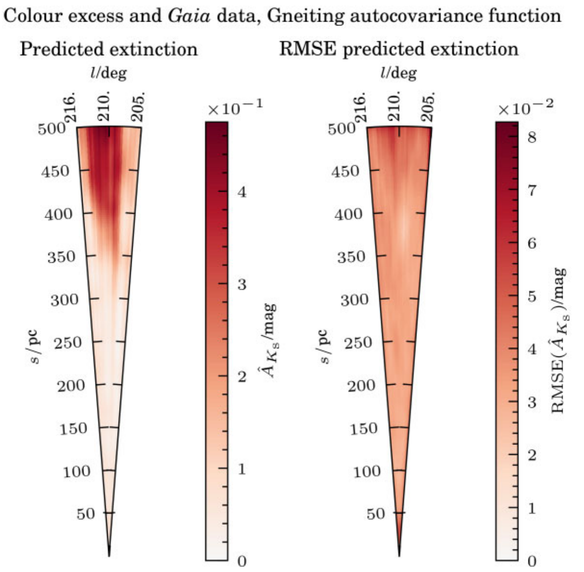

Figure 22. Colour excess and *Gaia* data: Predicted extinctions, $\hat{A}_{K_s}$, and their RMSEs, RMSE($\hat{A}_{K_s}$), computed using the Gneiting function equation (35), for the plane $b = -19.5$ deg. (See Section 6 for discussion. Cp. Fig. 10, which shows predictions computed using the Kolmogorov-like function.)

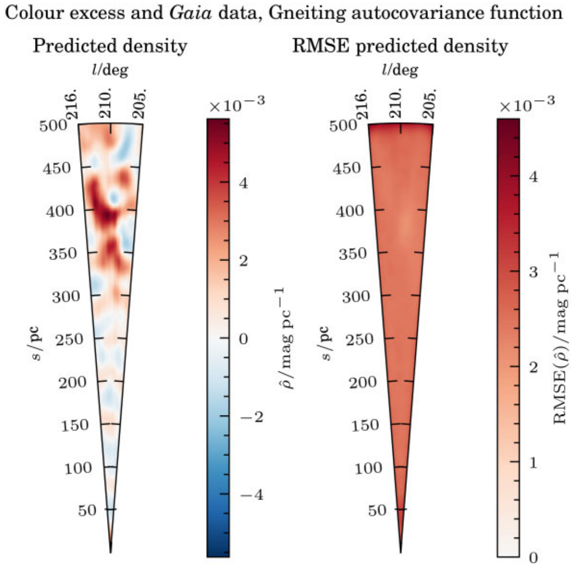

Figure 23. Colour excess and *Gaia* data: Predicted density, $\hat{\rho}$, and their RMSEs, RMSE($\hat{\rho}$), computed using the Gneiting function (equation 35), for the plane $b = -19.5$ deg. (See Section 6 for discussion. Cp. Fig. 11, which shows predictions computed using the Kolmogorov-like function.)

ACKNOWLEDGEMENTS

We gratefully acknowledge the support of the UKRI Science and Technology Facilities Council (grant ST/S000488/1). We would like to thank Sara Rezaei Kh., for generously making the data of her 2022 paper available to us, and our anonymous reviewer, whose insightful comments significantly improved this publication.

This publication makes use of data products from the Two Micron All Sky Survey, which is a joint project of the University of Massachusetts and the Infrared Processing and Analysis Center/California Institute of Technology, funded by the National Aeronautics and Space Administration and the National Science Foundation.

This publication makes use of data products from the Wide-field Infrared Survey Explorer, which is a joint project of the University of California, Los Angeles, and the Jet Propulsion Laboratory/California Institute of Technology, and NEOWISE, which is a project of the Jet Propulsion Laboratory/California Institute of Technology. WISE and NEOWISE are funded by the National Aeronautics and Space Administration.

This publication makes use of data from the European Space Agency (ESA) mission *Gaia* (https://www.cosmos.esa.int/gaia), processed by the *Gaia* Data Processing and Analysis Consortium (DPAC, https://www.cosmos.esa.int/web/gaia/dpac/consortium). Funding for the DPAC has been provided by national institutions, in particular the institutions participating in the *Gaia* Multilateral Agreement.

DATA AVAILABILITY

The RJCE extinctions used in this paper were provided by Sara Rezaei Kh. The StarHorse catalogue and the catalogue of Bailer-Jones are availabe at the *Gaia*Archive (https://gea.esac.esa.int/archive/) and the Gaia DR2 mirror archive (gaia.aip.de). Predictions of extinction and density were made using code written in Python. This code is available on request.

REFERENCES

Adler R. J., 1981, The Geometry of Random Fields. J. Wiley, Chichester, p. 25
Anders F. et al., 2019, A&A, 628, A94
Anders F. et al., 2021, A&A, 658, A91
Arenou F., Grenon M., Gomez A., 1992, A&A, 258, 104
Astraatmadja T. L., Bailer-Jones C. A. L., 2016a, ApJ, 832, 137
Astraatmadja T. L., Bailer-Jones C. A. L., 2016b, ApJ, 833, 119
Bailer-Jones C. A. L., 2011, MNRAS, 411, 435
Bailer-Jones C. A. L., 2015, PASP, 127, 994
Bailer-Jones C. A. L., Rybizki J., Fouesneau M., Mantelet G., Andrae R., 2018, AJ, 156, 58
Bailer-Jones C. A. L., Rybizki J., Fouesneau M., Demleitner M., Andrae R., 2021, AJ, 161, 147
Berry M. et al., 2012, ApJ, 757, 166
Binney J. et al., 2014, MNRAS, 439, 1231
Bouy H., Alves J., Bertin E., Sarro L. M., Barrado D., 2014, A&A, 564, A29
Burnett B., Binney J., 2010, MNRAS, 407, 339
Cardelli J. A., Clayton G. C., Mathis J. S., 1989, ApJ, 345, 245
Carpenter J. M., 2000, AJ, 120, 3139
Chen B. Q. et al., 2014, MNRAS, 443, 1192
Coles P., Barrow J. D., 1987, MNRAS, 228, 407
Cressie N., 1993, Statistics for Spatial Data, Wiley series in Probability And Statistics. J. Wiley, New York, p. 105
Dharmawardena T. E., Bailer-Jones C. A. L., Fouesneau M., Foreman-Mackey D., 2022, A&A, 658, A166
Draine B. T., 2011, Physics of the Interstellar and Intergalactic Medium. Princeton Univ. Press, Princeton, p. 113
Drimmel R., Cabrera-Lavers A., López-Corredoira M., 2003, A&A, 409, 205
Enßlin T. A., Frommert M., 2011, Phys. Rev. D, 83, 105014
Enßlin T. A., Weig C., 2010, Phys. Rev. E, 82, 51112
Gaia Collaboration, 2016, A&A, 595, A1
Gaia Collaboration, 2021, A&A, 649, A1
Gneiting T., 2002, J. Multivariate Anal., 83, 493
Goldberger A. S., 1962, J. Am. Stat. Assoc., 57, 369
Green G. M. et al., 2014, ApJ, 783, 114
Green G. M. et al., 2015, ApJ, 810, 25
Green G. M. et al., 2018, MNRAS, 478, 651
Green G. M., Schlafly E., Zucker C., Speagle J. S., Finkbeiner D., 2019, ApJ, 887, 93
Großschedl J. E. et al., 2018, A&A, 619, A106
Großschedl J. E. et al., 2019, A&A, 622, A149
Kounkel M. et al., 2018, AJ, 156, 84
Lada C. J., Lada E. A., Clemens D. P., Bally J., 1994, ApJ, 429, 694
Lallement R., 2015, J. Phys.: Conf. Ser., 577, 12016
Lallement R., Vergely J.-L., Valette B., Puspitarini L., Eyer L., Casagrande L., 2014, A&A, 561, A91
Lallement R. et al., 2018, A&A, 616, A132
Lallement R., Babusiaux C., Vergely J. L., Katz D., Arenou F., Valette B., Hottier C., Capitanio L., 2019, A&A, 625, A135
Leike R. H., Enßlin T. A., 2019, A&A, 631, A32
Leike R. H., Glatzle M., Enßlin T. A., 2020, A&A, 639, A138
Lombardi M., 2009, A&A, 493, 735
Lombardi M., Alves J., 2001, A&A, 377, 1023
Majewski S. R., Zasowski G., Nidever D. L., 2011, ApJ, 739, 25
Marshall D. J., Robin A. C., Reylé C., Schultheis M., Picaud S., 2006, A&A, 453, 635
Megeath S. T. et al., 2012, AJ, 144, 192
Megeath S. T. et al., 2015, AJ, 151, 5
Meingast S. et al., 2016, A&A, 587, A153
Meingast S., Alves J., Lombardi M., 2018, A&A, 614, A65
Ostriker E. C., Stone J. M., Gammie C. F., 2001, ApJ, 546, 980
Queiroz A. B. A. et al., 2018, MNRAS, 476, 2556
Rasmussen C. E., 2006, Gaussian Processes for Machine Learning. MIT, Cambridge, p. 14
Rezaei Kh. S., Kainulainen J., 2022, ApJ, 930, L22
Rezaei Kh S., Bailer-Jones C. A. L., Hanson R. J., Fouesneau M., 2017, A&A, 598, A125
Rezaei Kh S., Bailer-Jones C. A. L., Schlafly E. F., Fouesneau M., 2018, A&A, 616, A44
Rezaei Kh S., Bailer-Jones C. A. L., Soler J. D., Zari E., 2020, A&A, 643, A151
Sale S. E., 2012, MNRAS, 427, 2119
Sale S. E., 2015, MNRAS, 452, 2960
Sale S. E., Magorrian J., 2014, MNRAS, 445, 256
Sale S. E. et al., 2014, MNRAS, 443, 2907
Santiago B. X. et al., 2016, A&A, 585, A42
Schlafly E. F. et al., 2015, ApJ, 799, 116
Skrutskie M. F. et al., 2006, AJ, 131, 1163
Tennekes H., 1972, A First Course in Turbulence. MIT Press, p. 210
Vergely J.-L., Freire Ferrero R., Siebert A., Valette B., 2001, A&A, 366, 1016
Vergely J.-L., Valette B., Lallement R., Raimond S., 2010, A&A, 518, A31
Wang K. A., Pleiss G., Gardner J. R., Tyree S., Weinberger K. Q., Wilson A. G., 2019, Adv. Neural Inf. Process. Syst., 32, 14622
Wright E. L. et al., 2010, AJ, 140, 1868

APPENDIX A: COMPUTING THE PREDICTED DENSITY

Our predictor for the density at a point, $\hat{\rho}(\boldsymbol{r})$ (equation 23), is the derivative of the BLUP of the extinction at that point, $\hat{A}(\boldsymbol{r})$. To compute it, note that in equation (20) only $\boldsymbol{\gamma}$ and σ are functions of s, so that

$$\hat{\rho}(\boldsymbol{r}) = \frac{\partial \boldsymbol{\gamma}^{\rm t}}{\partial s}\boldsymbol{A} + \frac{\partial \sigma^{\rm t}}{\partial s}\boldsymbol{\Sigma}^{-1}(\boldsymbol{A} - \boldsymbol{\Gamma}^{\rm t}\boldsymbol{A}) \tag{A1}$$

where

$$\frac{\partial \boldsymbol{\gamma}}{\partial s} = \boldsymbol{\Sigma}^{-1}\Phi^{\rm t}(\Phi\boldsymbol{\Sigma}^{-1}\Phi^{\rm t})^{-1} \tag{A2}$$

and $[\partial\sigma/\partial s]_i = {\rm cov}(\rho(\boldsymbol{r}), A(\boldsymbol{r}_i))$. Alternatively, we may rewrite the BLUP of the extinction as $\hat{A}(\boldsymbol{r}) = \boldsymbol{\alpha}^{\rm t}\boldsymbol{A}$ where

$$\boldsymbol{\alpha} = (\boldsymbol{I} - \boldsymbol{\Gamma})\boldsymbol{\Sigma}^{-1}\sigma + \boldsymbol{\gamma}, \tag{A3}$$

in which case our predictor of density may be rewritten as

$$\hat{\rho}(\boldsymbol{r}) = \frac{\partial \boldsymbol{\alpha}^{\rm t}}{\partial s}\boldsymbol{A}. \tag{A4}$$

This involves the same partial derivative, $\partial \boldsymbol{\alpha}/\partial s$, that is involved in the expression for $\mathrm{var}(\rho(\boldsymbol{r}) - \hat{\rho}(\boldsymbol{r}))$ (equation B9). Note that

$$\frac{\partial \boldsymbol{\alpha}}{\partial s} = (\boldsymbol{I} - \boldsymbol{\Gamma})\boldsymbol{\Sigma}^{-1}\frac{\partial \sigma}{\partial s} + \frac{\partial \boldsymbol{\gamma}}{\partial s}, \tag{A5}$$

which equips us with all the information we need to compute $\hat{\rho}(\boldsymbol{r})$ and its prediction interval (Appendix B).

APPENDIX B: PREDICTION INTERVALS AND THE DISTRIBUTION OF THE BLUP

A prediction interval for $\hat{A}(\boldsymbol{r})$ is

$$[\hat{A}(\boldsymbol{r}) - \lambda_A S_A, \hat{A}(\boldsymbol{r}) + \lambda_A S_A] \tag{B1}$$

where

$$S_A := \sqrt{\mathrm{var}(A(\boldsymbol{r}) - \hat{A}(\boldsymbol{r}))} \tag{B2}$$

and λ_A is a critical value for the random variable $A(\boldsymbol{r}) - \hat{A}(\boldsymbol{r})$. Because $\hat{A}(\boldsymbol{r})$ is unbiased the variance of $A(\boldsymbol{r}) - \hat{A}(\boldsymbol{r})$ is equal to the mean-square error of $\hat{A}(\boldsymbol{r})$ since

$$\mathrm{MSE}(\hat{A}(\boldsymbol{r})) = \mathrm{var}(A(\boldsymbol{r}) - \hat{A}(\boldsymbol{r})) + \mathrm{bias}^2(\hat{A}(\boldsymbol{r})) \tag{B3}$$

$$= \mathrm{var}(A(\boldsymbol{r}) - \hat{A}(\boldsymbol{r})). \tag{B4}$$

This mean-square error is the quantity minimized by the BLUP of the extinction, and is given by Goldberger (1962) as

$$\begin{aligned}\mathrm{MSE}(\hat{A}(\boldsymbol{r})) = {} & \mathrm{var}(A(\boldsymbol{r})) - \sigma^{\mathrm{t}}\boldsymbol{\Sigma}^{-1}\sigma \\ & + (\boldsymbol{\phi} - \Phi\boldsymbol{\Sigma}^{-1}\sigma)^{\mathrm{t}}(\Phi\boldsymbol{\Sigma}^{-1}\Phi^{\mathrm{t}})^{-1}(\boldsymbol{\phi} - \Phi\boldsymbol{\Sigma}^{-1}\sigma).\end{aligned} \tag{B5}$$

Similarly, a prediction interval for $\hat{\rho}(\boldsymbol{r})$ is

$$[\hat{\rho}(\boldsymbol{r}) - \lambda_\rho S_\rho, \hat{\rho}(\boldsymbol{r}) + \lambda_\rho S_\rho] \tag{B6}$$

where

$$S_\rho := \sqrt{\mathrm{var}(\rho(\boldsymbol{r}) - \hat{\rho}(\boldsymbol{r}))} \tag{B7}$$

and λ_ρ is a critical value for the random variable $\rho(\boldsymbol{r}) - \hat{\rho}(\boldsymbol{r})$. Using equations (20) and (23) we find that this variance is

$$\begin{aligned}\mathrm{var}(\rho(\boldsymbol{r}) - \hat{\rho}(\boldsymbol{r})) = {} & \mathrm{var}(\rho(\boldsymbol{r})) + \mathrm{var}(\hat{\rho}(\boldsymbol{r})) \\ & - 2\,\mathrm{cov}(\rho(\boldsymbol{r}), \hat{\rho}(\boldsymbol{r}))\end{aligned} \tag{B8}$$

$$= \sigma^2_{\Delta\rho} + \frac{\partial \boldsymbol{\alpha}^{\mathrm{t}}}{\partial s}\boldsymbol{\Sigma}\frac{\partial \boldsymbol{\alpha}}{\partial s} - 2\,\mathrm{cov}(\rho(\boldsymbol{r}), \boldsymbol{A})\frac{\partial \boldsymbol{\alpha}}{\partial s} \tag{B9}$$

where the derivative $\partial \boldsymbol{\alpha}/\partial s$ is computed in Appendix A. A confidence interval for μ_ρ is

$$[\hat{\mu}_\rho - \lambda_{\mu_\rho} S_{\mu_\rho}, \hat{\mu}_\rho + \lambda_{\mu_\rho} S_{\mu_\rho}] \tag{B10}$$

where

$$S_{\mu_\rho} := \sqrt{\mathrm{var}(\hat{\mu}_\rho)} \tag{B11}$$

and λ_{μ_ρ} is a critical value for $\hat{\mu_\rho}$. This variance is

$$\mathrm{var}(\hat{\mu}_\rho) = (\boldsymbol{\Phi}^{\mathrm{t}}\boldsymbol{\Sigma}^{-1}\boldsymbol{\Phi})^{-1}. \tag{B12}$$

To find the critical values λ_A, λ_ρ, and λ_{μ_ρ} we must know the distributions of $A(\boldsymbol{r}) - \hat{A}(\boldsymbol{r})$, $\rho(\boldsymbol{r}) - \hat{\rho}(\boldsymbol{r})$, and $\hat{\mu}_\rho$ respectively. But, as we have observed, the BLUP requires us to have knowledge only of the first and second moments of $(A(\boldsymbol{r}), \boldsymbol{A})$. In fact, this is one of the principal benefits of the method. If we do not know this distribution then we do not know the distributions of $A(\boldsymbol{r}) - \hat{A}(\boldsymbol{r})$, $\rho(\boldsymbol{r}) - \hat{\rho}(\boldsymbol{r})$, and $\hat{\mu}_\rho$. Instead, we can find limits for the prediction intervals using Chebyshev's inequality, which holds for all distributions. In this situation, the 68-95-99.7 rule for normal random variables does not hold. Instead, the confidence levels 0.68, 0.95, and 0.997 are associated with upper limits on the critical values of 1.77, 4.47, and 18.3 rather than the usual values of 1, 2, and 3.

APPENDIX C: VALIDATION OF THE MAPS

Validation of the BLUP is crucial, and the process of validation helps weed out predictors that underperform. The predictors of extinction that we construct using RJCE extinction data combined with line-of-sight distances inferred by Bailer-Jones et al. (2021) pass validation. But those that we construct using StarHorse data (Anders et al. 2019) do not. We plot the standardized leave-one-out residuals for these predictors in Figs C1 and C2. We do not expect the residuals to have Gaussian distribution, but they must obey Chebyshev's inequality (see Appendix B).

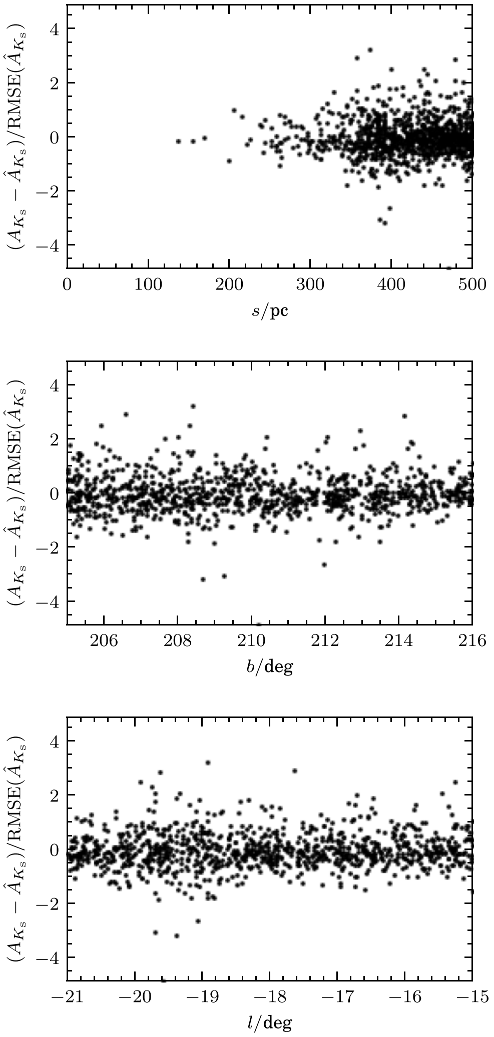

Figure C1. Colour excess and *Gaia* data: The standardized leave-one-out residuals of the predicted extinction. (For the sake of clarity these plots show a sample of size 1000, uniformly distributed in volume.)

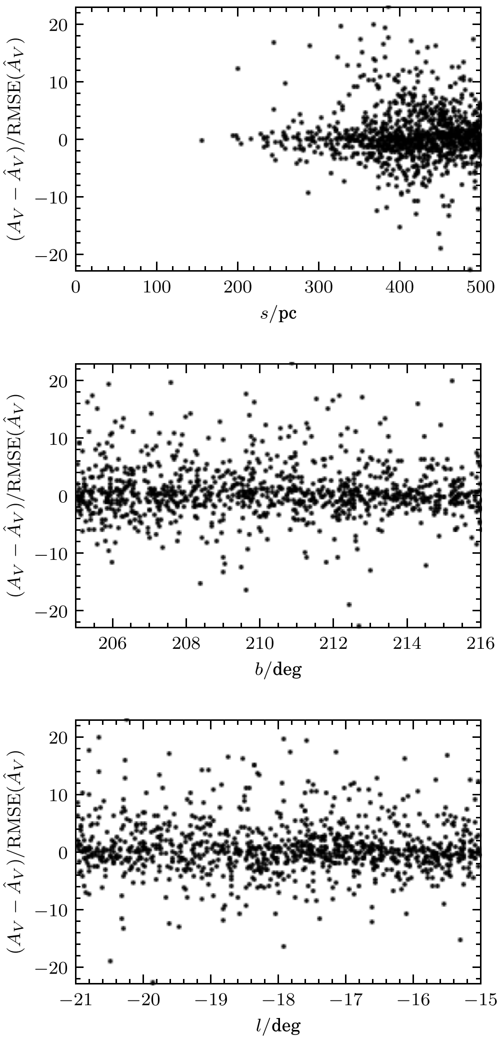

Figure C2. StarHorse data: The standardized leave-one-out residuals of the predicted extinction. (For the sake of clarity these plots show a sample of size 1000, uniformly distributed in volume.)

APPENDIX D: THE AUTOCOVARIANCE FUNCTIONS

We have introduced the functions f and g (equations 16 and 17), which give the covariance of two points drawn from the density and extinction fields in terms of their line-of-sight distances and angular separation. We plot these functions in Figs D1–D5 for $\Omega = 1$ and $\gamma = 11/3$ under the assumption of unit variance, $\sigma^2_{\Delta\rho}$, and unit length scale, L_0. For a given angular separation, θ_{12}, the functions f and g are both symmetric in s_1 and s_2. In the case that $\theta = 0$ deg, the diagonals give the variance at a line-of-sight distance $s_1 = s_2$, while in the case of $\theta_{12} > 0$ deg the origins give the variance, and the diagonals give the covariance at a common distance.

For all values of θ, the function f is peaked on the diagonal, and approximately zero far from it. For $\theta = 0$ deg it is constant along the diagonal, and for $\theta > 0$ deg it decreases along the diagonal from a maximum at the origin. The greater the angular separation, the faster it decreases. This behaviour is seen most clearly seen in Fig. D3, which shows f for fixed s_1 and θ_{12} and variable s_2.

For $\theta = 0$ deg, the function g is linear in s_1 and constant in s_2 above the diagonal. Below the diagonal it is constant in s_1 and linear in s_2. This is to say that, along a line of sight, the extinction at a point is strongly correlated with the extinction at a second point more distant since that extinction must be at least as great, and decreasingly correlated with the extinction at a point less distant, since that extinction must be smaller. There is a smooth transition across the diagonal, most clearly seen in Fig. D4, the width of which is approximately L_0. This smooth transition is due to the fact that densities, and hence extinctions, are strongly correlated at distances of order L_0 or less, whether the second point is more or less distant than the first. For $\theta > 0$ deg, the function g above the diagonal is linear in s_1 up to some critical value and constant in s_1 beyond that critical value, whilst being constant in s_2. Below the diagonal the function g is constant in s_1, whilst being linear in s_2 up to the critical value and constant in s_2 beyond the critical value. The greater the angular separation, the smaller the linear regime. Along distinct lines of sight, the extinction at a point is less strongly correlated with the extinction at a second point more distant since that extinction need not be as great and decreasingly correlated with the extinction at a point less distant since that extinction must again be zero at the origin. Again, there is a smooth transition across the diagonal, more clearly in Fig. D4, due to the fact that extinctions are strongly correlated at distances of order L_0 or less.

D1 Alternative covariance functions

We have also discussed the use of autocovariance functions that have no direct physical motivation, and in particular the use of the squared-exponential and Gneiting functions (Section 6). In Fig. D6 we show the graphs of these, alongside the Kolmogorov-like autocovariance function, all for the case of unit variance and unit characteristic length scale.

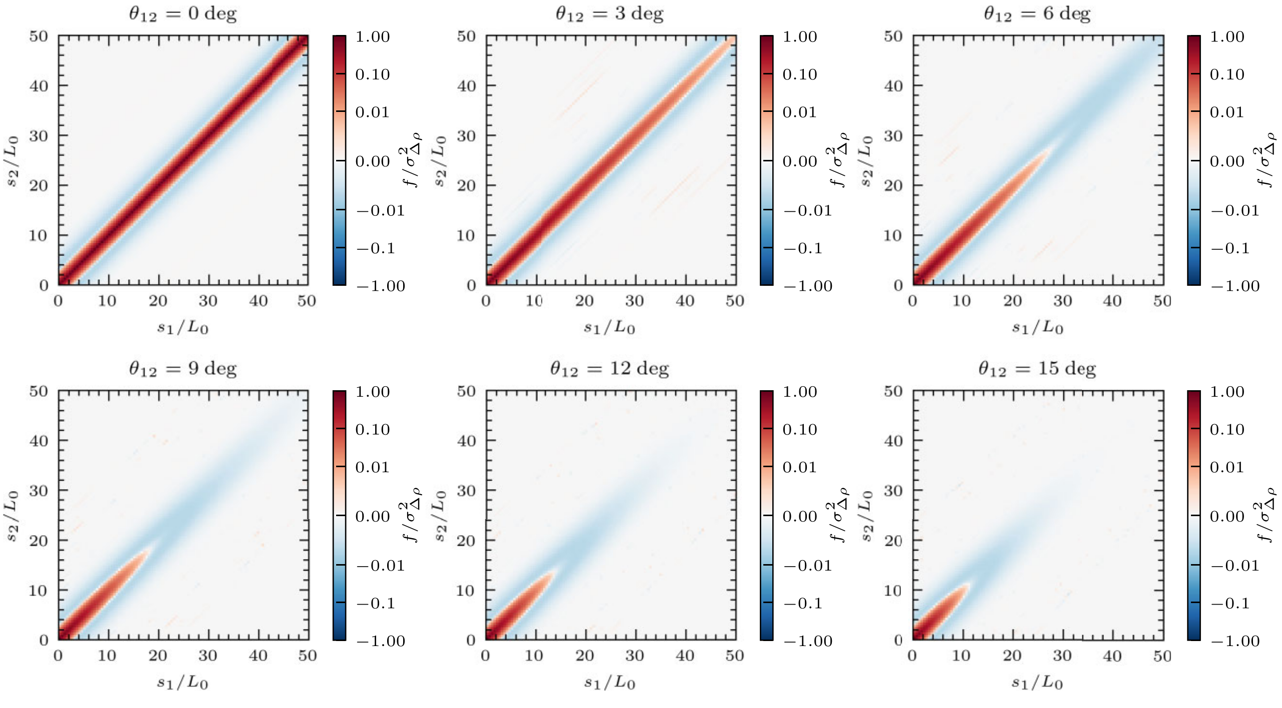

Figure D1. Covariance of the density of the ISM at two points, $\boldsymbol{r}_1$ and $\boldsymbol{r}_2$, as a function of the distances, s_1 and s_2, and the angular separation, θ_{12} (the function *f*; equation 16) for $\Omega = 1$ and $\gamma = 11/3$. In each panel the angular separation is fixed, and the distances allowed to vary. The covariance is shown on an arcsinh scale with linear width 0.001.

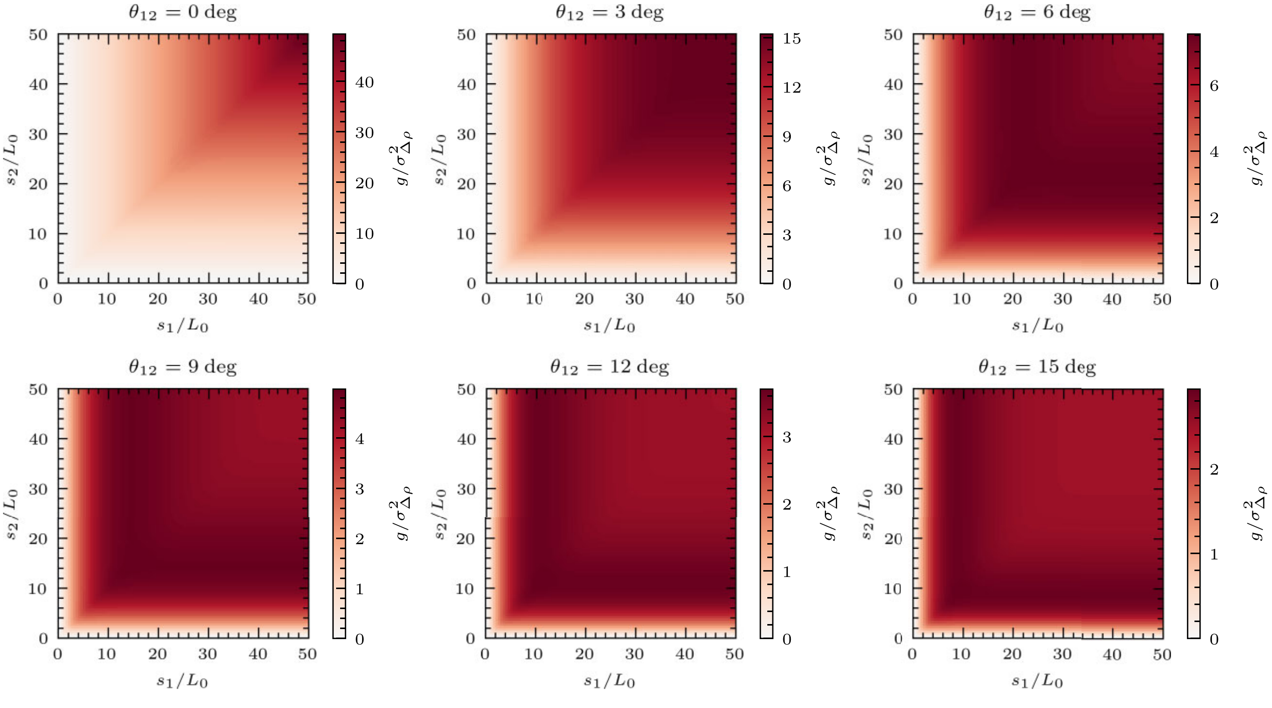

Figure D2. Covariance of the extinction at two points, $\boldsymbol{r}_1$ and $\boldsymbol{r}_2$, as a function of the distances, s_1 and s_2, and the angular separation, θ_{12} (the function g, equation 17) for $\Omega = 1$ and $\gamma = 11/3$. In each panel the angular separation is fixed, and the distances allowed to vary.

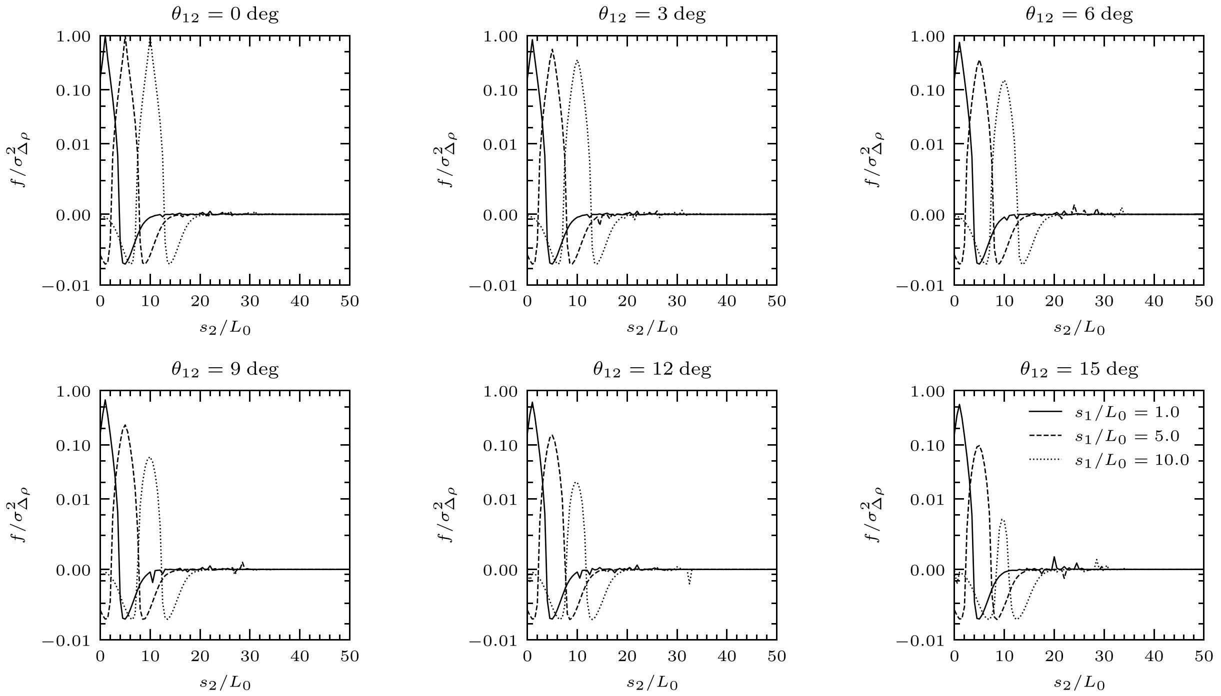

Figure D3. Covariance of the density of the ISM at two points, $\boldsymbol{r}_1$ and $\boldsymbol{r}_2$, as a function of the distances, s_1 and s_2, and the angular separation, θ_{12} (the function *f*, equation 16) for $\Omega = 1$ and $\gamma = 11/3$. In each panel the distance s_1 and the angular separation are fixed, and the distance s_2 allowed to vary. The covariance is shown on an arcsinh scale with linear width 0.001.

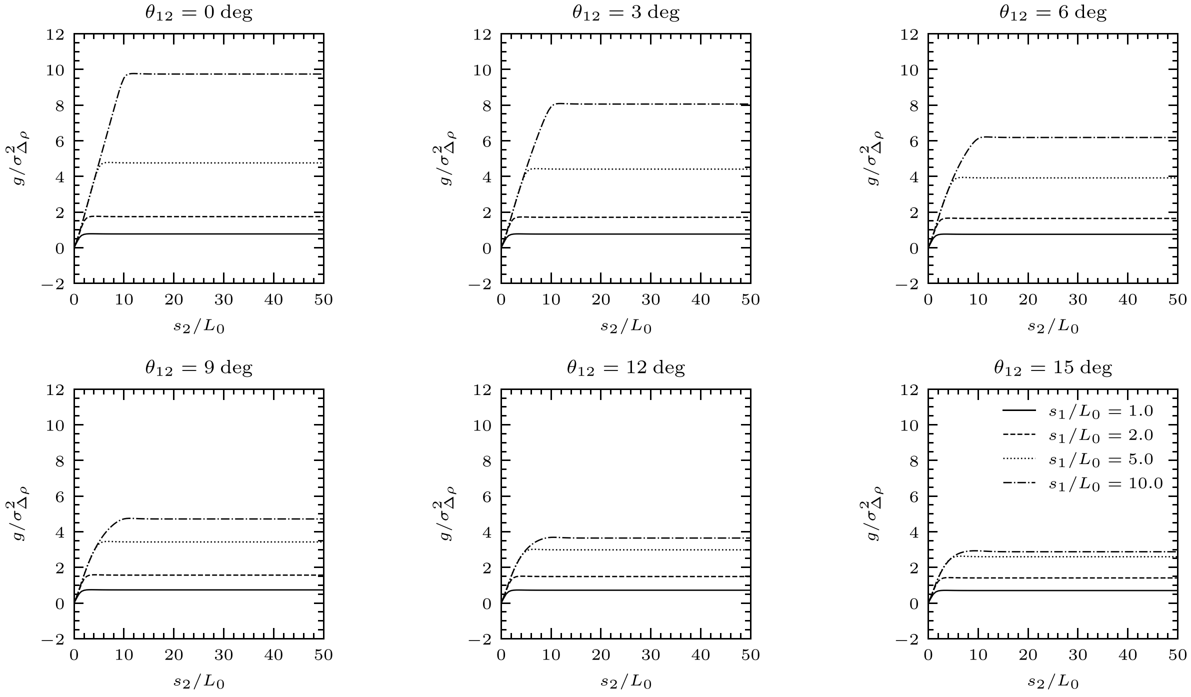

Figure D4. Covariance of the extinction at two points, $\boldsymbol{r}_1$ and $\boldsymbol{r}_2$, as a function of the distances, s_1 and s_2, and the angular separation, θ_{12} (the function *g*, equation 17) for $\Omega = 1$ and $\gamma = 11/3$. In each panel the distance s_1 and the angular separation are fixed, and the distance s_2 allowed to vary.

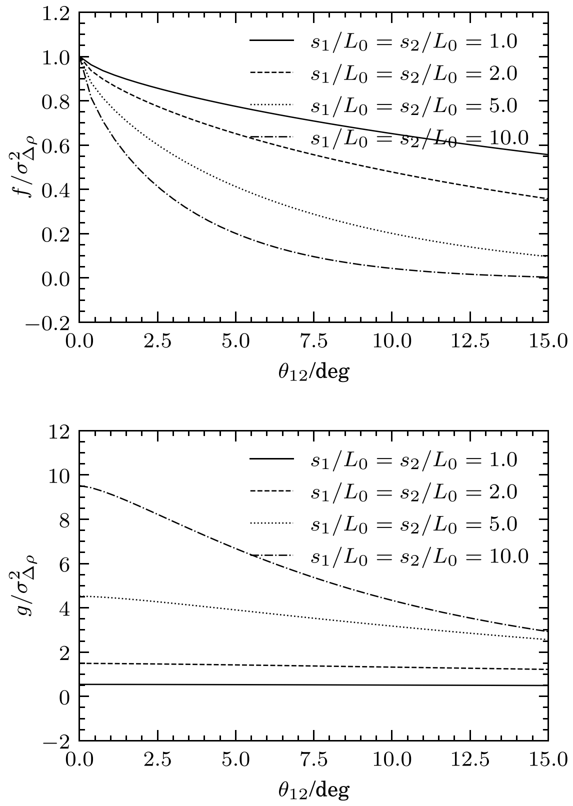

Figure D5. Covariance of the density of the ISM (top, the function f, equation 16) and of the extinction (bottom, the function g, equation 17) for $\Omega = 1$, $\gamma = 11/3$, and unit length scale, L_0. See also Figs D1, D3, D2, and D4 and their captions. In each panel the distances s_1 and s_2 are equal and the angular separation, θ_{12}, allowed to vary.

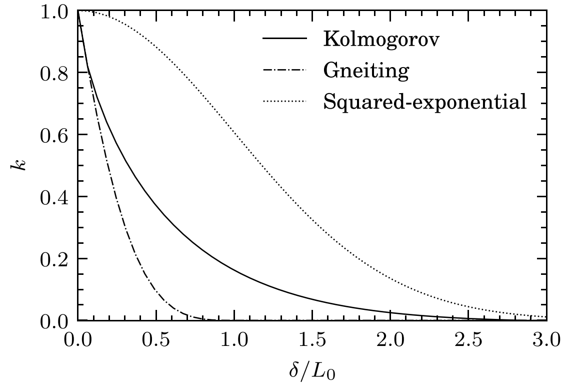

Figure D6. The squared-exponential autocovariance function, k_{PE} (equation 34; $\alpha = 2$), Gneiting autocovariance function, k_{G} (equation 35), and Kolmogorov-like autocovariance function, $k_{\Delta\rho}$ (equations 8 and 9), for the case of unit variance and unit characteristic length scale. The Kolmogorov-like autocovariance function has power-law indices $\Omega = 1$ and $\gamma = 11/3$.

This paper has been typeset from a TEX/LATEX file prepared by the author.